LA-UR-17-28074

Title: Cyclops I: Modeling Error Study for Inertially Confined Detonation of Insensitive High Explosive (IHE) PBX-9502

Author(s): Hughes, Justin Matthew
Terrones, Guillermo
Shores, Erik Frederick

Intended for: Report

Issued: 2018-04-02 (rev.1)

CYCLOPS I: Modeling Error Study for Inertially Confined Detonation of Insensitive High Explosive (IHE) PBX-9502

Justin M. Hughes, Guillermo Terrones, Erik Shores
jhughes@lanl.gov, terrones@lanl.gov, eshores@lanl.gov
X-Theoretical Design, Safety and Surety

Table of Contents

Abstract

A validation study is performed using the hydrodynamics code PAGOSA to assess the accuracy of reflected shock, burn front propagation, and Photon Doppler Velocimetry (PDV) predictions using several burn models and strength models. Experimental data collected from proton radiography (pRad) is compared to burn front propagation times and reflected shock patterns. Burn front isochrones are computed and the lag time for the burn front is quantified for a given burn model. The effect of strength models and damage are assessed by comparison of simulations to experimental PDV data.

Summary of Work

The following tasks were completed with this study:

- Experimental burn front data from Photon Radiography (pRad) compared to PAGOSA simulations using Scaled Unified Reactive Front (SURF), Forest Fire (FF), and Multishock Forest Fire (MSFF) burn models by quantifying simulation burn front time-of-arrival via artificial viscosity.

- Experimental Photon Doppler Velocimetry (PDV) data compared to simulated PDV signals for the outer stainless steel confinement using the Johnson-Cook (JC), KOSPALL, Preston-Tonks-Wallace (PTW), and Steinberg-Cochran-Guinan (SG) strength models with and without Johnson-Spall damage enabled

Introduction

The concept of Verification and Validation (V&V) plays a role in ensuring that the modeling of physical phenomenon via complex computer simulations is not only correct, but that the underlying physics are adequately captured. Here, verification means to ensure that you are solving the correct problem; that is, you are solving the correct set of physically representative mathematical equations with an adequate representation of the specific boundary conditions to an appropriate degree. Model validation means that your models have been checked against other independently validated implementations or rigorously compared to physical experiments.

Two major aspects of V&V are determining both accuracy and precision of a computational metric of interest by assessing the variation of the result due to variations in modeling inputs. Accuracy, or systematic bias, describes the difference between the mean value of the simulation's output domain with respect to the "true" value, which may be a well-established computational metric or physical experiment. Precision describes the statistical distribution of the possible answers in the model output domain.

The problem for this study is a complex High Explosive (HE) shock propagation and detonation validation experiment called CYCLOPS. An example of the geometry, reproduced from [1], is shown in Figure 1. Due to the geometry, many factors important to the modeling of HE may be tested at once, namely the Equation of State (EOS) that describes the pressure behind a shock, the burn model that converts the reactants to products and supplies the energy that drives the shock, and the effect of material strength on the degree of HE confinement. By being able to accurately capture the resulting reflected shock patters and burn front times, both the EOS and burn model pair may be validated from a series of experiments.

Burn front and reflected shock data were quantified from experiments using proton radiographic techniques at the Los Alamos Neutron Science Center (LANSCE) in a series of shots [2]. References [1,3,4,5,6] contain experimental data obtained from these CYCLOPS shots.

The following sections address the ideas behind the Cyclops experiments and the analysis techniques used.

There are three experimental setups in the CYCLOPS series: CYCLOPS I with PBX-9502, CYCLOPS II with PBX-9501, and CYCLOPS III with LX-04. This report focuses on CYCLOPS I with PBX-9502, SS-304L stainless steel outer confinement, and tin inner confinement. The current study focuses on a precursory analysis of model accuracy for CYCLOPS I by analyzing the differences in simulation results using a bevy of strength models and burn models to describe the stainless steel confinement cylinder and PBX-9502, respectively. Root-mean-square (RSS) errors are computed and will be used as the basis for determining the minimum error simulation. Once the best strength model and burn model combination is determined, an Uncertainty Quantification (UQ) and Sensitivity Analysis (SA) will be performed in a future study.
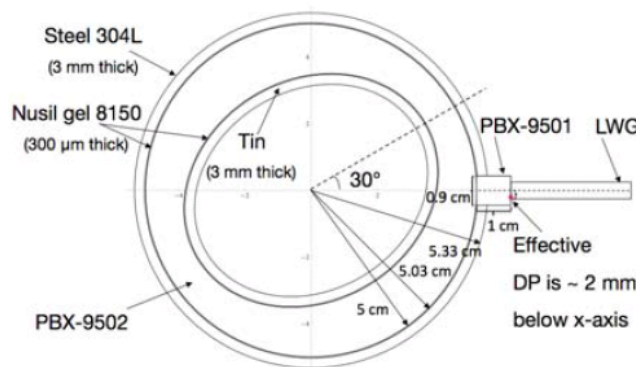
Figure 1. Cross-section view of the CYCLOPS shot geometry showing the steel cylinder and tin ellipsoidal cylinder confinement of the PBX-9502 [1].

CYCLOPS I: Insensitive High Explosive (IHE) PBX-9502 Experiment

A pair of CYCLOPS shots were performed to characterize the PBX-9502. An initial proof shot was executed to check for the potential of damaging the photon radiography (pRad) equipment to be used to track the propagation of the burn front and reflected shocks and was fielded with 8 Photon Doppler Velocimeters (PDVs) [1]. Once it was determined that the shot was safe for the pRad equipment, a second shot was performed at the LANCSE facility [REFERENCE].

Proof Shot

An initial proof shot was performed to assess the possibility of the formation of an axial jet that could damage the pRad equipment. PDV sensors were fielded to track the motion of the outer cylindrical shell. The experimental setup for the proof shot is available in Figure 2.
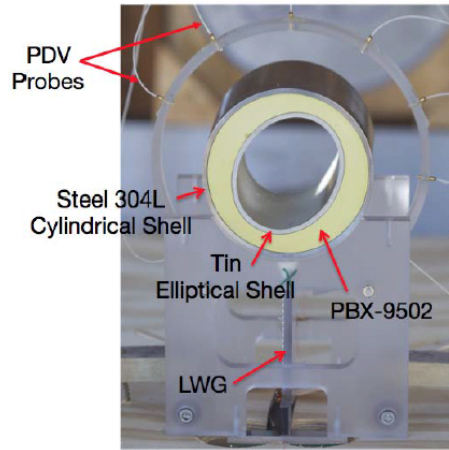
Figure 2. Experimental setup of the CYCLOPS I shot showing the locations of the PDV sensors and live wave generator (LWG) [1]

A total of eight PDV sensors were fielded with one Velocity Interferometer System for Any Reflector (VISAR) probe for the pRad shot as seen in Figure 3. A summary of the data garnered from this experiment is shown in Figure 4. As a note, the PDV timing in Figure 4 is relative to the nominal load ring. By subtracting 0.924±0.005 μs, the timing can be made relative to the Current Viewing Resistor (CVR) and by adding the detonator CVR to the breakout time, the PDV timing can be made relative to the breakout. However, due to the unknown timing difference between the experiment and simulation, for all comparisons of PDV signals simulation timing is adjusted to best fit the experimental data. Also, due to the complex nature of colliding shocks, the 15th isochrone for both the upper and lower regions are excluded from all analyses.
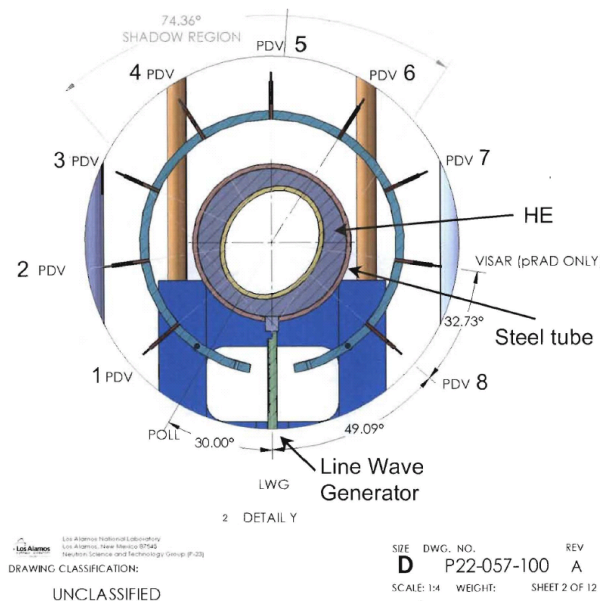
Figure 3. PDV and VISAR probe locations for the CYCLOPS I proof shot [4]
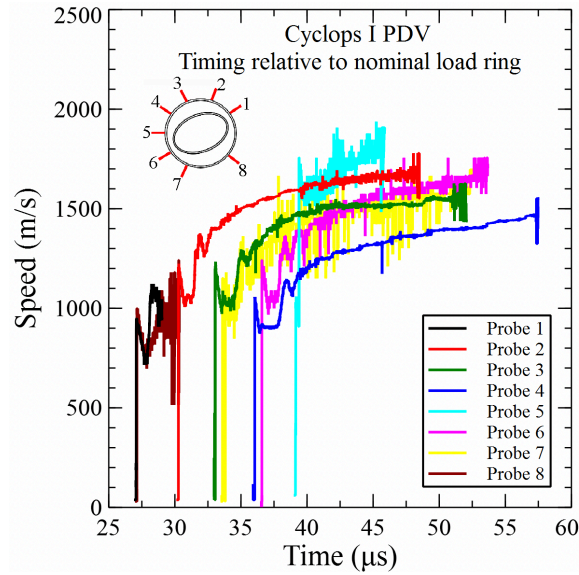
Figure 4. PDV data from the CYLOPS I proof shot for timing relative to the nominal load ring [4].

Proton Radiography

Burn front and reflected shocks visible from proton radiography experiments were measured from in-situ radiographs. An example of the burn fronts and reflected shocks as seen from pRad experiments is shown in Figure 5. Tables 1 and 2 give the isochrones position data garnered from the pRad experiments for the upper and lower region, repectively. Isochrones are numbered one to 15 starting closest to the booster as per Figure 6 [3].
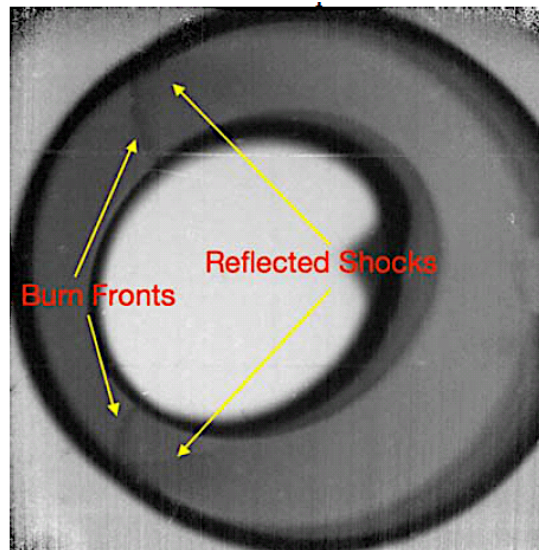
Figure 5. pRad radiograph at approximately 13.8 µs after booster ignition showing burn fronts and reflected shocks

5
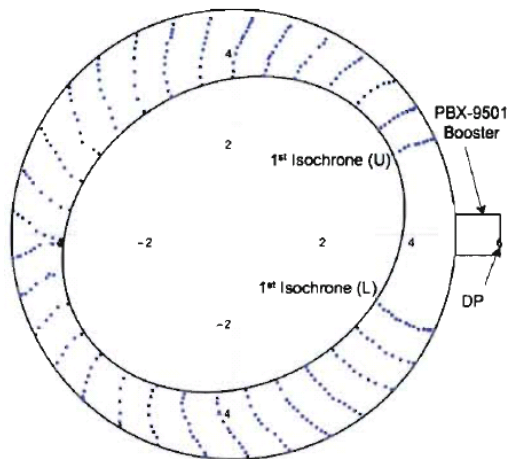
Figure 6. Isochrone positions showing numbering starting closest to the PBX-9501 booster

Table 1. Isochrone position data for the upper portion ($0 \leq \theta \leq \pi$) of the CYCLOPS geometry

1st Isochrone t=3.8 µs		2nd Isochrone t=4.8 µs		3rd Isochrone t=5.8 µs		4th Isochrone t=6.8 µs		5th Isochrone t=7.8 µs	
X	Y	X	Y	X	Y	X	Y	X	Y
3.58	1.78	3.30	2.38	2.80	2.92	2.19	3.34	1.36	3.47
3.74	1.85	3.40	2.43	2.91	3.06	2.30	3.46	1.43	3.61
3.84	1.93	3.50	2.52	3.08	3.18	2.39	3.58	0.50	3.74
3.93	1.98	3.59	2.59	3.22	3.28	2.50	3.67	1.60	3.82
4.08	2.01	3.69	2.64	3.37	3.35	2.60	3.74	1.71	3.96
4.16	2.03	3.79	2.70	3.49	3.37	2.71	3.81	1.91	4.17
4.27	2.05	3.89	2.73	3.59	3.40	2.80	3.87	2.02	4.25
4.35	2.09	3.97	2.77			2.86	3.93	2.06	4.34
4.44	2.12	4.02	2.78						
4.50	2.13	4.05	2.80						
		4.06	2.81						

| 6th Isochrone t=8.8 µs		7th Isochrone t=9.8 µs		8th Isochrone t=10.8 µs		9th Isochrone t=11.8 µs		10th Isochrone t=12.8 µs	
X	Y	X	Y	X	Y	X	Y	X	Y
0.67	3.52	-0.04	3.49	-0.71	3.33	-1.40	3.06	-2.01	2.73
0.72	3.65	-0.02	3.63	-0.75	3.50	-1.47	3.19	-2.17	3.01
0.70	3.79	-0.02	3.81	-0.76	3.73	-1.51	3.39	-2.22	3.31
0.77	3.90	0.04	4.01	-0.74	3.93	-1.57	3.58	-2.22	3.61
0.81	3.97	0.07	4.15	-0.70	4.11	-1.55	3.79	-2.25	3.93
0.87	4.05	0.14	4.26	-0.67	4.24	-1.55	3.94	-2.23	4.14
0.95	4.18	0.18	4.35	-0.63	4.37	-1.51	4.08	-2.20	4.27
1.04	4.31	0.21	4.42	-0.60	4.49	-1.50	4.25	-2.18	4.43
1.09	4.40	0.27	4.51	-0.57	4.68	-1.42	4.38		
1.16	4.51	0.31	4.59	-0.53	4.78	-1.40	4.48		
1.22	4.59	0.35	4.68	-0.52	4.80	-1.38	4.55		
1.26	4.63	0.39	4.30			-1.37	4.67		
		0.41	4.78						

11th Isochrone t=13.8 µs		12th Isochrone t=14.8 µs		13th Isochrone t=15.8 µs		14th Isochrone t=16.8 µs		15th Isochrone t=17.8 µs	
X	Y	X	Y	X	Y	X	Y	X	Y
-2.65	2.38	-3.02	1.79	-3.44	1.20	-3.69	0.55	-3.90	-0.13
-2.73	2.59	-3.15	1.89	-3.65	1.31	-3.88	0.61	-4.07	-0.80
-2.80	2.81	-3.40	2.05	-3.80	1.49	-4.11	0.76	-4.25	-0.02
-2.91	3.04	-3.46	2.26	-3.91	1.67	-4.33	0.94	-4.43	0.08
-2.99	3.22	-3.51	2.54	-4.04	1.83	-4.51	1.15	-4.58	0.20
-3.02	3.43	-3.57	2.70	-4.11	1.97	-4.59	1.26	-4.74	0.37
-3.04	3.64	-3.65	2.98	-4.20	2.09	-4.67	1.34	-4.85	0.45
-3.06	3.77	-3.69	3.12	-4.25	2.22	-4.71	1.41	-4.96	0.52
-3.04	3.91	-3.70	3.27	-4.33	2.34				
		-3.70	3.35						

Table 2. Isochrone postion data for the lower portion (-π ≤ θ ≤ 0) of the CYCLOPS geometry

1st Isochrone t=3.8 μs		2nd Isochrone t=4.8 μs		3rd Isochrone t=5.8 μs		4th Isochrone t=6.8 μs		5th Isochrone t=7.8 μs	
X	Y	X	Y	X	Y	X	Y	X	Y
3.29	-1.56	2.80	-2.09	2.24	-2.58	1.63	-2.94	0.99	-3.29
3.38	-1.67	2.88	-2.19	2.33	-2.70	1.68	-3.03	1.06	-3.44
3.49	-1.72	3.01	-2.31	2.49	-2.82	1.76	-3.13	1.20	-3.67
3.57	-1.80	3.14	-2.38	2.61	-2.92	1.84	-3.23	1.27	-3.75
3.65	-1.88	3.29	-2.52	2.72	-3.03	1.96	-3.34	1.36	-3.85
3.75	-1.92	3.42	-2.64	2.86	-3.12	2.07	-3.45	1.45	-3.92
3.88	-1.97	3.58	-2.70	3.05	-3.24	2.16	-3.56	1.56	-4.04
3.97	-2.03	3.77	-2.79	3.20	-3.31	2.24	-3.64	1.67	-4.12
4.05	-2.06	3.95	-2.84	3.43	-3.39	2.38	-3.71	1.76	-4.20
4.16	-2.11	4.06	-2.87	3.57	-3.44	2.50	-3.77	1.88	-4.29
4.28	-2.12					2.62	-3.85	1.98	-4.36
4.38	-2.13					2.74	-3.90	2.08	-4.41
4.44	-2.13					2.86	-4.00	2.17	-4.47

6th Isochrone t=8.8 μs		7th Isochrone t=9.8 μs		8th Isochrone t=10.8 μs		9th Isochrone t=11.8 μs		10th Isochrone t=12.8 μs	
X	Y	X	Y	X	Y	X	Y	X	Y
0.29	-3.46	-0.36	-3.65	-1.06	-3.56	-1.71	-3.37	-2.46	-3.20
0.33	-3.61	-0.36	-3.76	-1.12	-3.64	-1.81	-3.80	-2.54	-3.43
0.40	-3.81	-0.31	-3.95	-1.15	-3.76	-1.85	-3.67	-2.55	-0.37
0.50	-4.01	-0.22	-4.16	-1.12	-3.92	-1.89	-3.81	-2.54	-3.99
0.57	-4.12	-0.12	-4.32	-1.08	-4.07	-1.89	-4.01	-2.55	-4.16
0.64	-4.21	-0.06	-439.00	-0.99	-4.21	-1.83	-0.27	-2.54	-4.25
0.78	-4.33	0.02	-4.51	-0.95	-4.38	-1.78	-4.40		
0.94	-4.45	0.14	-4.65	-0.89	-4.51	-1.71	-4.52		
1.07	-4.58	0.21	-4.74	-0.80	-4.60	-1.69	-4.69		
1.17	-4.70	0.29	-4.84	-0.74	-4.71				
1.26	-4.80	0.33	-4.94	-0.64	-4.86				
				-0.62	-4.92				

11th Isochrone t=13.8 μs		12th Isochrone t=14.8 μs		13th Isochrone t=15.8 μs		14th Isochrone t=16.8 μs		15th Isochrone t=17.8 μs	
X	Y	X	Y	X	Y	X	Y	X	Y
-2.98	-2.68	-3.40	-2.22	-3.72	-1.55	-4.03	-0.91	-3.91	-0.24
-3.07	-2.78	-3.56	-2.31	-3.95	-1.63	-4.14	-0.89	-4.07	-0.21
-3.19	-2.98	-3.75	-2.51	-4.09	-1.79	-4.20	-0.97	-4.35	-0.23
-3.25	-3.15	-3.83	-2.68	-4.20	-1.91	-4.43	-1.10	-4.48	-0.31
-3.30	-3.30	-3.96	-2.86	-4.37	-2.09	-4.56	-1.23	-4.56	-0.36
-3.35	-3.49			-4.43	-2.23	-4.66	-1.31	-4.67	-0.42
-3.38	-3.61					-4.75	-1.34	-4.79	-0.47
-3.36	-3.70					-4.79	-1.37	-4.85	-0.49
								-4.96	-0.53

Simulation Analysis Methods

Simulation Metric

The computed burn fronts and reflected shocks are assessed by the lag time of the numerical simulation versus experiment [1]; that is, the difference in the time taken for the computed burn front or the reflected shock to reach the same location of the experiment is quantified. This is represented by the equation:

$$\Delta\tau(t_{exp}, s) = t_{mQ}(\theta_{exp}, s) - t_{exp} \tag{1}$$

where t_{exp} is the time taken for the experimental front to reach a specific location, θ_{exp} is the angular position of the front at time t_{exp}, and s is a dimensionless parameter in the range ($0 \leq s \leq 1$) for a parameterized polar function that describes the area of the HE. A parameterized polar function is used that scales from an ellipse to a circle of the form:

$$h = \frac{(a + s)(b + cs)}{[(a + s)^2 sin^2(\theta - 30°) + (b + cs)^2 cos^2(\theta - 30°)]^{1/2}} \tag{2}$$

where a = 4, b = 3.3359, and c = 1.6641. At s = 0, this gives an inclined ellipse at 30 °with major and minor axes of 4 cm and 3.3359 cm, respectively. At s = 1, this gives a circle of radius 5 cm. This equation gives the radius from the center of the circle, *h*, at some *s* percent (between 0 and 1) distance between the interior elliptical cylinder and exterior circle at angle θ. Using this equation and transforming the (h, θ) coordinate pairs back to Cartesian coordinates, it is possible to seed the IHE region with tracer particles in a regularized grid for PAGOSA.

Using a grid of Eulerian tracer particles, the artificial viscosity, Q, can be tracked at explicit points in the (s,θ) domain as a function of time. For each tracer, when data is plotted versus simulation time, there are three peaks; the first peak is associated with the burn front while the remaining two are associated with reflected shock fronts. By extracting the simulation time for the first peak, the time for the burn front can be used to generate a function $t_{mQ} = F(\theta, s)$ that can be numerically inverted to compute the location, $\theta_I = F^{-1}(\theta, s)$, of an isochrone at t_I. By solving (2) for this computed angle and interpolating within the grid at discrete *s* positions for constant time t_I, radial positions along the constant-time burn front can be found.

PAGOSA Numerical Analysis

The finite difference hydrodynamics code PAGOSA was used to simulate the CYCLOPS I shot. A single Equation of State (EOS) was used to describe the pressure relationship for the reaction products of the PBX-9502. Huygens construction, Detonation Shock Dynamics (DSD), and Forest Fire (FF) burn models were used to compare the relative accuracy of each burn model implementation. In addition, for the Huygens construction programmed burn model, two distinct regions of the IHE were specified to differentiate regions beyond the line-of-sight of the detonator. A constant mesh size of 200 μm was used for each simulation. Since the FF model is mesh size dependent, multiple mesh sizes from 500 μm to 150 μm were tested for convergence. Figure 7 shows the isochrone lag times for the lower region (-π ≤ θ ≤ 0) of the CYCLOPS geometry for the FF burn model. Figure 8 shows the average lag time in shakes (0.01 μs) along each computed isochrone for simulations using the FF burn model.
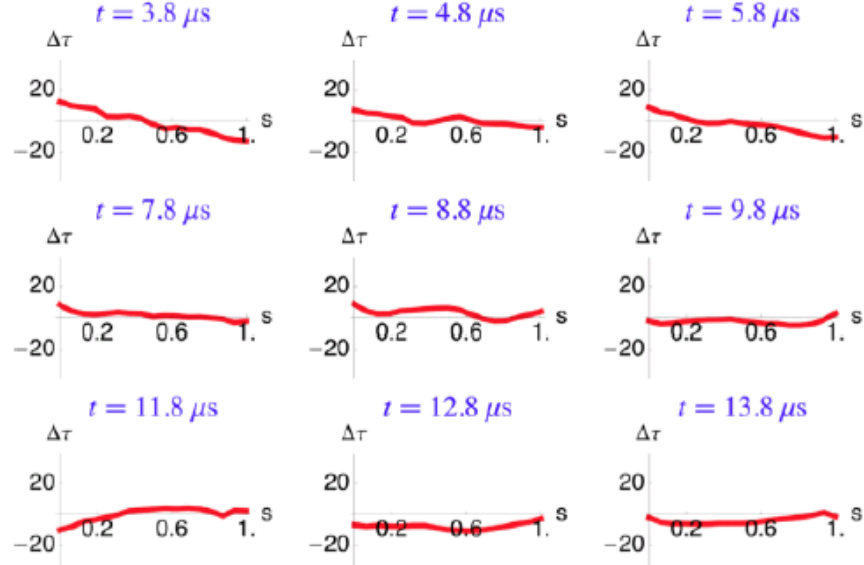
Figure 7. PAGOSA computed isochrone lag time metric for the FF burn model in the lower region of the CYCLOPS geometry (-π ≤ θ ≤ 0) for select isochrones.
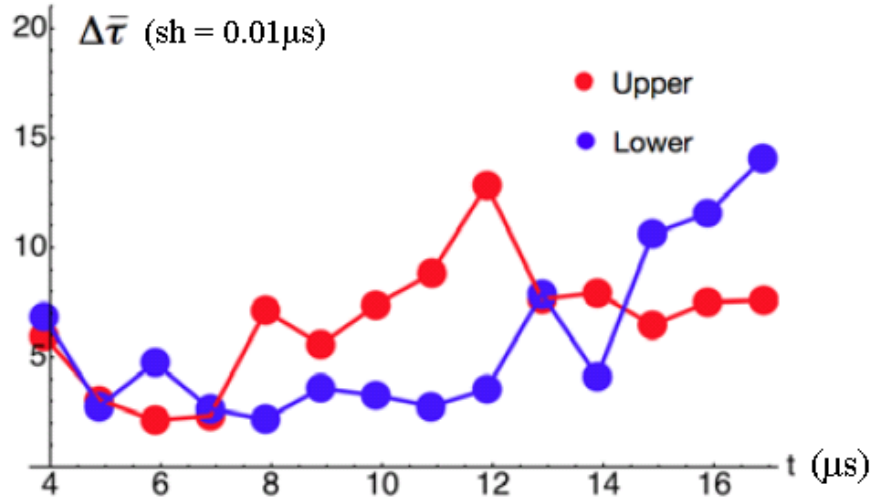
Figure 8. Spatial average ($\Delta\bar{\tau}$) over the range ($0 \leq s \leq 1$) of PAGOSA computed isochrone lag times for the upper ($0 \leq \theta \leq \pi$) and lower ($-\pi \leq \theta \leq 0$) regions of the CYCLOPS geometry versus simulation time.

As seen in Figure 8, for the first 14 μs the simulation is in good agreement with the experimental data for the lower region with an average difference of 8 shakes or less. After 14 μs, the lower region is less accurate than the upper region. The global average ⟨Δτ⟩ for the upper and lower regions are 6.6 shakes and 5.7 shakes, respectively. Table 3 shows a summary of the global average lag times for each burn model investigated. Overall, the DSD burn model gave the best results when compared to experimental data.

10

Table 3. Global average $\langle \Delta\tau \rangle$ lag times in shakes (sh = 0.01 µs) for different burn models

Burn Model	Upper Region	Lower Region	Global
No Shadow Fraction	21.6	26.1	23.9
0.95 Shadow Fraction	8.4	10.6	9.5
Two IHE Regions	6.3	9.6	8
DSD	3.8	8.4	6.1
Forest Fire	6.6	5.7	6.2

Detonation Wave Front Curvature Relationships

Expanding on the ideas presented by [1], [7] tested different relationships for the detonation velocity versus curvature $D(\kappa)$ of the detonation wave front. The same validation metric as [1] was employed. The following is a summary of the work performed by [7].

Simulations were performed in 2D and 3D configurations using in-house codes developed by Atomic Weapons Establishment (AWE). Two $D(\kappa)$ relations are tested form [8,9] along with a custom relation from rate stick data from Los Alamos National Laboratory (LANL) called the Swift relation [7]. The relationship of [8] (Aslam) extends DSD to include effects of front acceleration, time rate of change of shock normal direction, and transverse flow. The relationship of [9] (Hill), introduces dependencies on initial temperature, initial density, and the reaction zone thickness. Despite variations in the materials (recycled versus virgin) each relationship was calibrated to, the curvature relation calibration for PBX-9502 are relatively close, as seen in Figure 9 (reproduced from [7]).
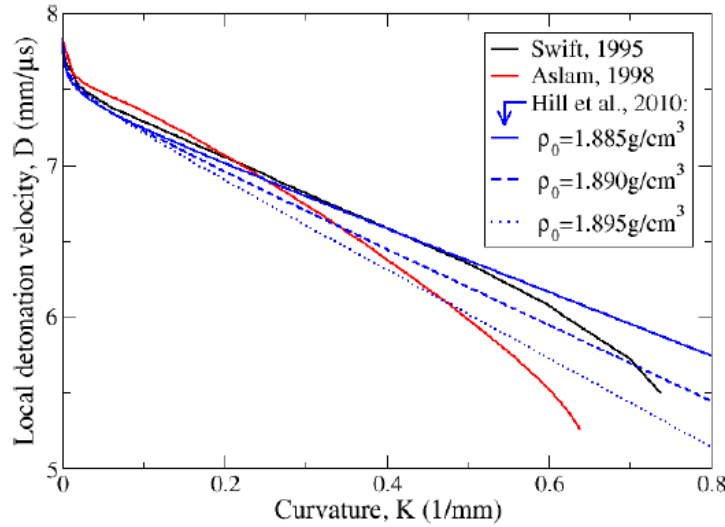
Figure 9. Local detonation velocity versus curvature relations for different lots of PBX-9502, reproduced from [7]

To account for the thin layer of gel between the PBX-9502 and the tin and steel confinement tubes, the boundary angles for the DSD $D(\kappa)$ relationships were set to fixed values: 58° for unconfined HE, 62° for tin confinement, and 65° for steel confinement. This effectively reduces the confinement of the tin and steel cylinders by limiting the curvature. These angles were estimated from steady-state detonation cylinder tests [10].

Two-dimensional and three-dimensional simulations were performed to compare the effects of the infinite depth assumption for the 2D simulations. The 3D model used the full geometry of the problem with a set depth of 10 cm with open boundary conditions for all mesh boundaries.

For the experiments performed by [1], the pRad detector was aimed down the long axis of the cylinder, effectively presenting an averaged density for the wave fronts. Since wave front curvature is mainly confined to the open ends fo the cylinder, measurements based on the radiographs introduces uncertainty in the timing. Future studies for DSD timing should account for this uncertainty. Table 4 shows the computed global average metric for the 2D DSD calculations using the three different $D(\kappa)$ relationships [7]. Figure 10 shows the global metric plots for two isochrones compared to isochrones computed for the Swift, Aslam, and Hill relationships [7]. According to the results for the Hill relationship, the variation of the lag time versus initial density demonstrated low sensitivity. The selection of the $D(\kappa)$ is considered to be the most dominant factor affecting the isochrone lag times while initial density is seen as second order.

The Swift relationship produced the best results for the 2D simulations with the main discrepancy being the lower region of the IHE where the timing is consistently ahead when compared to the experiments. This discrepancy increases with increasing simulation time. Since the detonation point was positioned 2mm below the center of the booster, this creates a sharper turning angle for the lower section and leads to a dead zone in the experiments which is not accounted for in the simulations.

Table 4. 2D simulation global average time metric, reproduced from [7]

$D(\kappa)$ Relation	$\langle \Delta\tau \rangle$ Upper (ns)	$\langle \Delta\tau \rangle$ Lower (ns)	Match
Swift	59	65	Balanced
Aslam	45	93	Too Fast
Hill (ρ_0 low to high)	89 / 92 / 96	51 / 47 /48	Too Slow
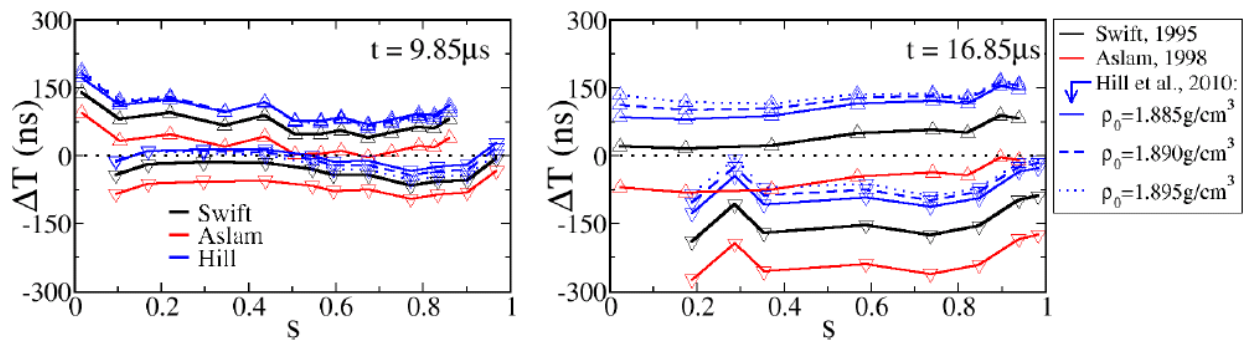
Figure 10. 2D DSD isochrone calculations for the three $D(\kappa)$ reltions. (Δ = upper region, ∇ = lower region)

Since the swift relation produced the best results for 2D simulations, the same relation was used to test how a 3D geometry would affect results. Overall, by switching to a 3D simulation, an average of 40 ns was added to the lag times. From the mid-plane wave front to the edge of the cylinder introduces a 110 ns delay. Though Aslam's relation produced consistently fast results in

2D, this is somewhat compensated for by switching to a 3D simulation. Aslam's relation produces the best match in 3D when compared to the experiments [7].

Burn Front Time Error

Continuing the work of [1], a mesh convergence study was performed to assess the accuracy of the Forest Fire (FF), Multi-Shock Forest Fire (MSFF), and Scaled Unified Reactive Front (SURF) burn models with respect to changes in mesh size. Mesh sizes of 150 μm, 200 μm, and 500 μm were used to examine the isochrone burn front times. To ensure minimal error in burn time estimations, the experimental isochrone positions were simulated as Eulerian tracers. Burn front times were estimated from the time-of-arrival of maximum artificial viscosity of each tracer. Each burn model used a dual form EOS with the Jones-Wilkins-Lee (JWL) equation of state used to describe the pressure relationship for the PBX-9502 reaction products and the Mie-Grüneisen relationship to describe the solid reactants. Table 5 gives a summary of the root-mean-square (RMS) error with respect to the experimental isochrone timing for the lower and upper regions. Since the SURF burn model did not present a local error minimum in the 150 μm to 500 μm range, a 75 μm mesh size simulation was run to determine if the simulation would further converge or exhibit the same divergent behavior as the FF burn model. Figure 11 shows the global RMS error with respect to mesh size for the FF, SURF, and MSFF burn models. Over the mesh size range of 300 μm to 500 μm, all the burn models exhibit a reduction in total RMS error, where the SURF model converges at 150 μm, the FF burn model converges at 200 μm, and the MSFF burn model converges at 300 μm with a spike in error below 200 μm.

Table 5. Summary of mesh convergence study results for FF, MSFF, and SURF

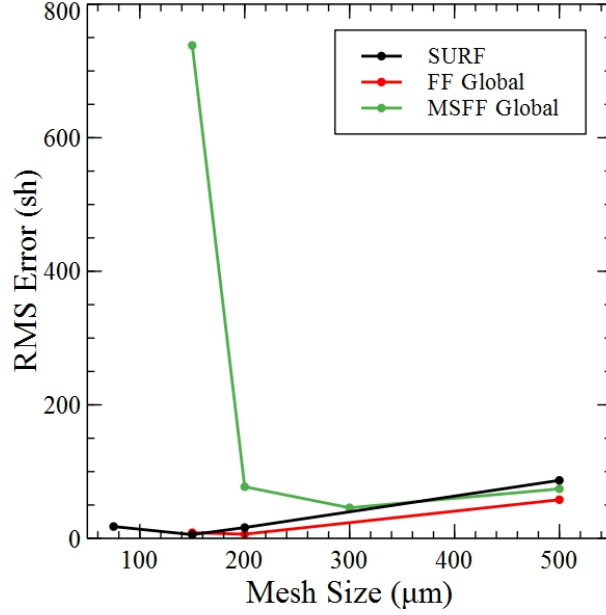| Mesh Size (μm)	Burn Model	Upper RMS Error (sh)	Lower RMS Error (sh)	Global RMS Error (sh)
150	FF	7.31	9.55	8.51
200	FF	8.46	2.95	6.33
500	FF	60.11	55.3	57.91
150	MSFF	740.08	736.44	738.26
200	MSFF	92.07	58.88	77.28
300	MSFF	47.4	44.26	45.85
500	MSFF	74.72	3.55	74.14
75	SURF	15.74	19.57	17.76
150	SURF	7.35	2.88	5.58
200	SURF	18.96	12.95	16.24
500	SURF	90.07	83.57	86.88

Figure 11. Global RMS error in shakes (sh) versus mesh size (μm) for the FF, SURF, and MSFF burn models

As noted by the summary of results in Table 5 and Figure 11, the FF burn model is more accurate than SURF at mesh sizes above 200 μm when comparing global RMS error. Table 6 gives the average isochrone lag times ($\Delta\tau$) for the most accurate mesh sizes (lowest RMS error) for the FF, MSFF, and SURF burn models.

Table 6. Isochrone lag times in shakes (sh) for the minimum error mesh sizes of each burn model

Burn Model	Mesh Size (μm)	Upper Region $\langle\Delta\tau\rangle$ (sh)	Lower Region $\langle\Delta\tau\rangle$ (sh)	Global $\langle\Delta\tau\rangle$ (sh)
FF	200	3.22	0.21	1.71
MSFF	300	42.94	43.29	43.12
SURF	150	3.33	0.44	1.89

Though the SURF burn model at 150 μm attains comparable accuracy to the FF burn model at 200 μm, the longer computational time for the SURF burn model at the finer mesh size may diminish its viability for longer simulations. Figure 12 shows the computational time versus mesh size for each burn model. Since the 75 μm simulations were run with 256 processors to reduce computational time, the performance for 64 processors was extrapolated using a power law data fit. Figure 13 shows the average lag time for each upper and lower isochrone using the most accurate mesh size for the FF, MSFF, and SURF burn models. The SURF and FF models are similar in average global timing and lag behind the experimental burn front timing while the MSFF model lags behind considerably. Based on the values of the RMS errors at each mesh size, the FF burn model using the dual form JWL/Mie-Grüneisen EOS best matches the experimental results.

14
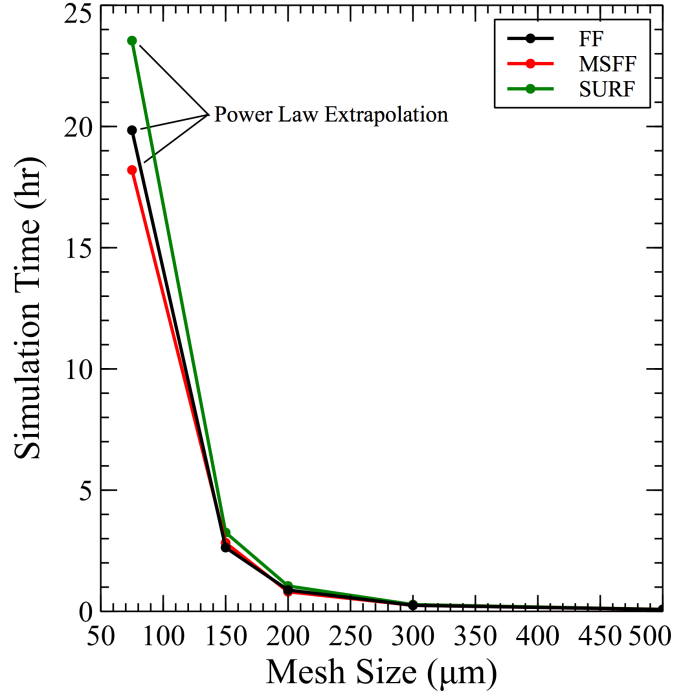
Figure 12. Simulation execution time versus mesh size for the FF, MSFF, and SURF burn models for simulations using 64 processors
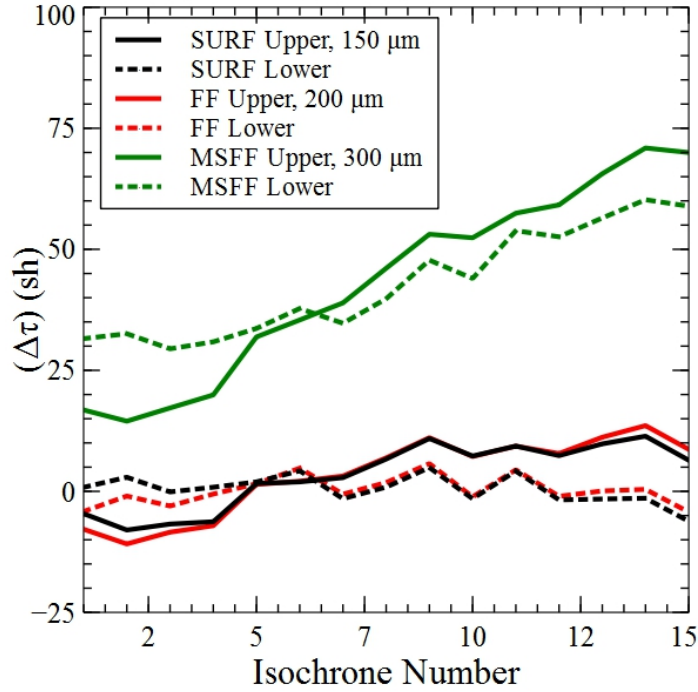
Figure 13. Average lag time in shakes (sh) for each isochrone in the upper and lower regions for the FF, MSFF, and SURF burn models

Photon Doppler Velocimetry (PDV) Error

To further asses the accuracy of the PAGOSA simulations with the newly implemented SURF burn model and test the energy transference from burn to kinetic drive, a series of simulations were performed to compare the simulated PDV data to CYCLOPS I experiments

(Figure 4). Four strength models were utilized to describe the strength relationship for the SS-304L: Modified Steinberg-Cochran-Guinan (SG) [11], Johnson-Cook (JC) [12], Kospall [13], and Preston-Tonks-Wallace (PTW) [14]. The effect of material damage on PDV signal predictions is also investigated using the Johnson-Spall (JS) [15] damage model for each strength model with a simple enabled/disabled scheme. Each strength model considered is strain rate and temperature dependent with differing relationships controlling their dependencies. All model constants are summarized in the appendix.

In order to directly compare the experimental and simulation data, the PDV signal timing delay must be equivalent. Unfortunately, no data exists such that an accurate experimental estimate of this timing difference can be made. Since the experimental timing is relative to the nominal load ring and the simulation timing is relative to the ignition of the PBX-9501 booster, the difference in timing will be inferred from the difference in the earliest velocity signal from both the experimental and simulated PDV signals. The simulated PDV that first generates a velocity signal is shifted to its corresponding experimental one. In this case, PDV 1 is the first channel to produce a velocity signal. Therefore, all simulated PDV signals are shifted up by the timing difference between PDV 1's experimental and simulated signals. A simple error minimization routine is used to find the timing difference that produces the minimum root-mean-square (RMS) error for PDV 1 for each strength model.

The following sections summarize the simulation results for each case considered. Each simulation uses a mesh size of 150 μm with the SURF burn model and the dual JWL/Mie-Grüneisen EOS for the PBX-9502. The error data from these figures are further condensed by calculating RMS error for the entire curve for a direct comparison between simulations.

Johnson-Cook (JC)

The Johnson-Cook strength model is a large-strain constitutive model based on the von Mises flow stress model [12] with sensitivity to applied strain rate and temperature. Figure 14 and Figure 15 directly compare the shifted PDV signals for the CYCLOPS I PAGOSA simulations using the Johnson-Cook strength model for the SS-304L confinement. The simulated PDV signals for this case are shifted by 20.227 μs.

In general, the model captures the initial velocity spike and subsequent drop. However, unlike the experimental data, each simulated PDV signal, with exception of PDV 5, exhibits a damped sinusoidal response as the pressure waves bounce between the inner and outer confinement cylinders. Figures 16 and 17 compare the same PAGOSA simulation with the Johnson-Cook model but with Johnson-Spall damage enabled. For the case with material damage, the PDV signals are shifted by 20.225 μs.

Figure 14. A comparison of experimental PDV signals with PAGOSA simulated PDVs for CYCLOPS I simulations using the Johnson-Cook strength model for SS-304L confinement for (a) PDV 1, (b) PDV 2, (c) PDV 3, and (d) PDV 4

JC

Figure 15. A comparison of experimental PDV signals with PAGOSA simulated PDVs for CYCLOPS I simulations using the Johnson-Cook strength model for SS-304L confinement for (a) PDV 5, (b) PDV 6 (c) PDV 7, and (d) PDV 8

Figure 16. A comparison of experimental PDV signals with PAGOSA simulated PDVs for CYCLOPS I simulations using the Johnson-Cook strength model with the Johnson-Spall damage model for SS-304L confinement for (a) PDV 1, (b) PDV 2, (c) PDV 3, and (d) PDV 4

Figure 17. A comparison of experimental PDV signals with PAGOSA simulated PDVs for CYCLOPS I simulations using the Johnson-Cook strength model with the Johnson-Spall damage model for SS-304L confinement for (a) PDV 5, (b) PDV 6, (c) PDV 7, and (d) PDV 8

Kospall

The Kospall strength model in PAGOSA is a variation of the Steinberg-Cochran-Guinan [11] model with additional thermal softening terms and is strain rate and temperature dependent. Figure 18 and Figure 19 directly compare the shifted PDV signals for the CYCLOPS I PAGOSA simulations using the Kospall strength model for the SS-304L confinement. The PDV signals are shifted by 20.220 μs.

Again, each simulated PDV signal, with the exception of PDV 5, captures the initial velocity spike and shows a dampened sinusoidal response. Figures 20 and 21 compare the same PAGOSA simulation with the Kospall model but with Johnson-Spall damage enabled. For the case with material damage, the PDV signals are shifted by 20.225 μs.
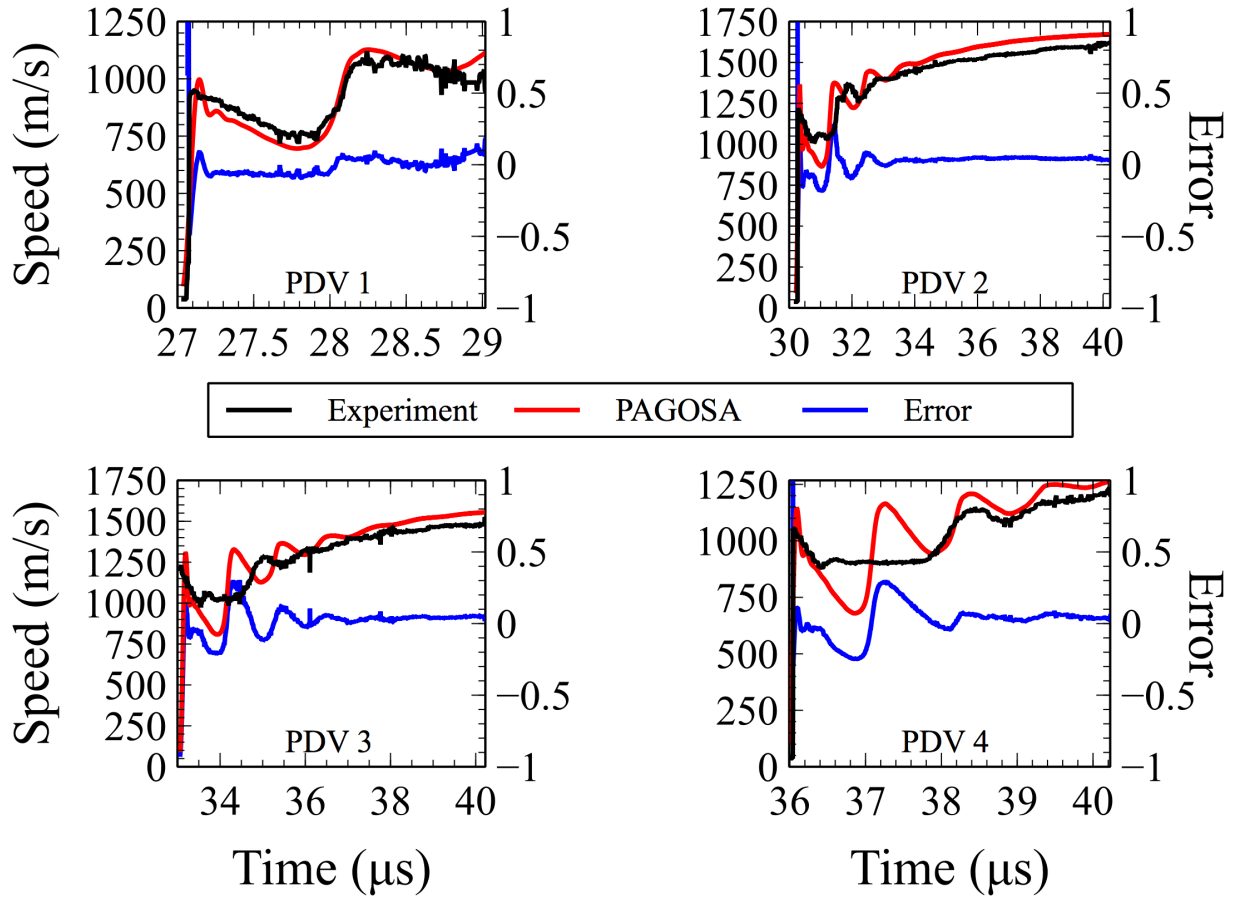
Kospall

Figure 18. A comparison of experimental PDV signals with PAGOSA simulated PDVs for CYCLOPS I simulations using the Kospall strength model for SS-304L confinement for (a) PDV 1, (b) PDV 2, (c) PDV 3, and (d) PDV 4
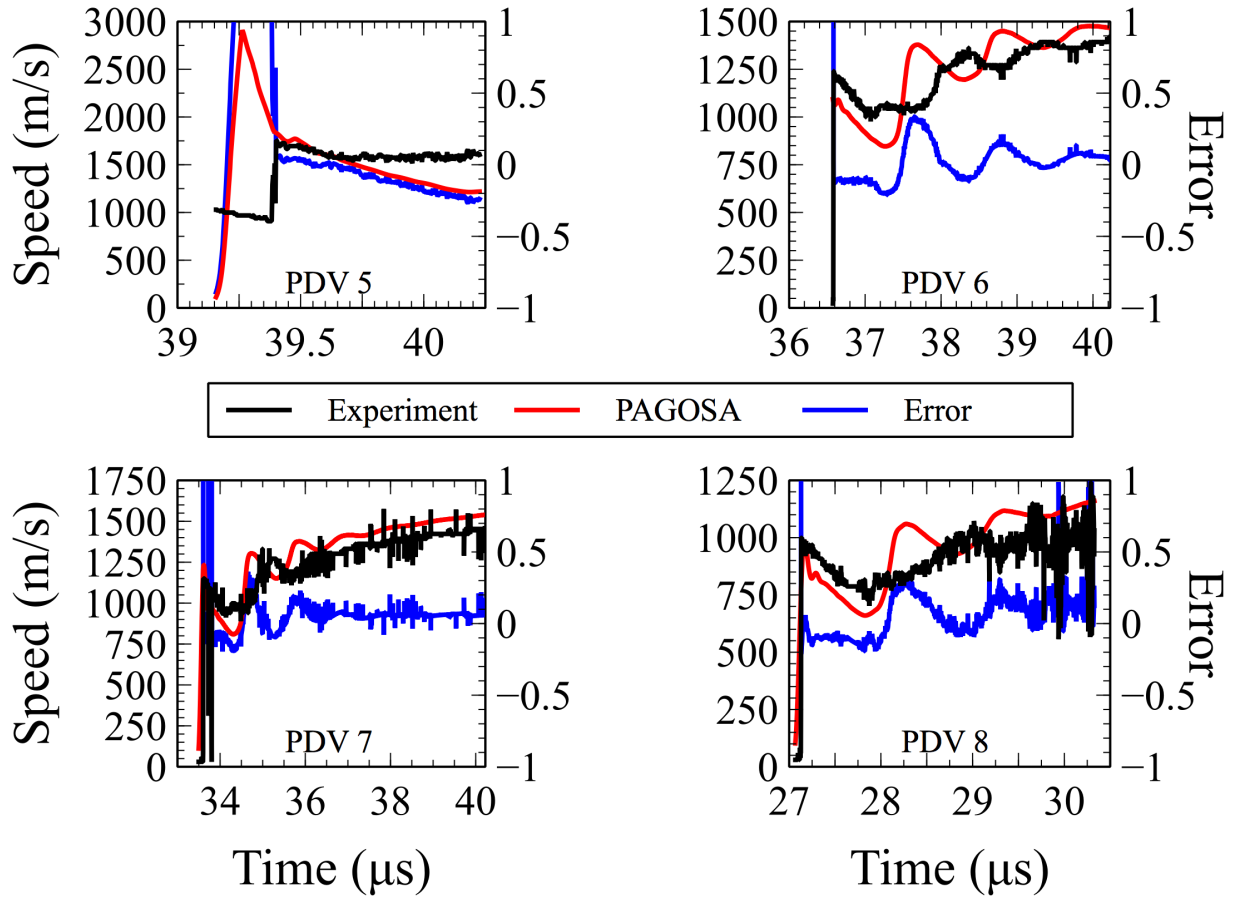
Figure 19. A comparison of experimental PDV signals with PAGOSA simulated PDVs for CYCLOPS I simulations using the Kospall strength model for SS-304L confinement for (a) PDV 5, (b) PDV 6 (c) PDV 7, and (d) PDV 8

Kospall+JS

Figure 20. A comparison of experimental PDV signals with PAGOSA simulated PDVs for CYCLOPS I simulations using the Kospall strength model with the Johnson-Spall damage model for SS-304L confinement for (a) PDV 1, (b) PDV 2, (c) PDV 3, and (d) PDV 4
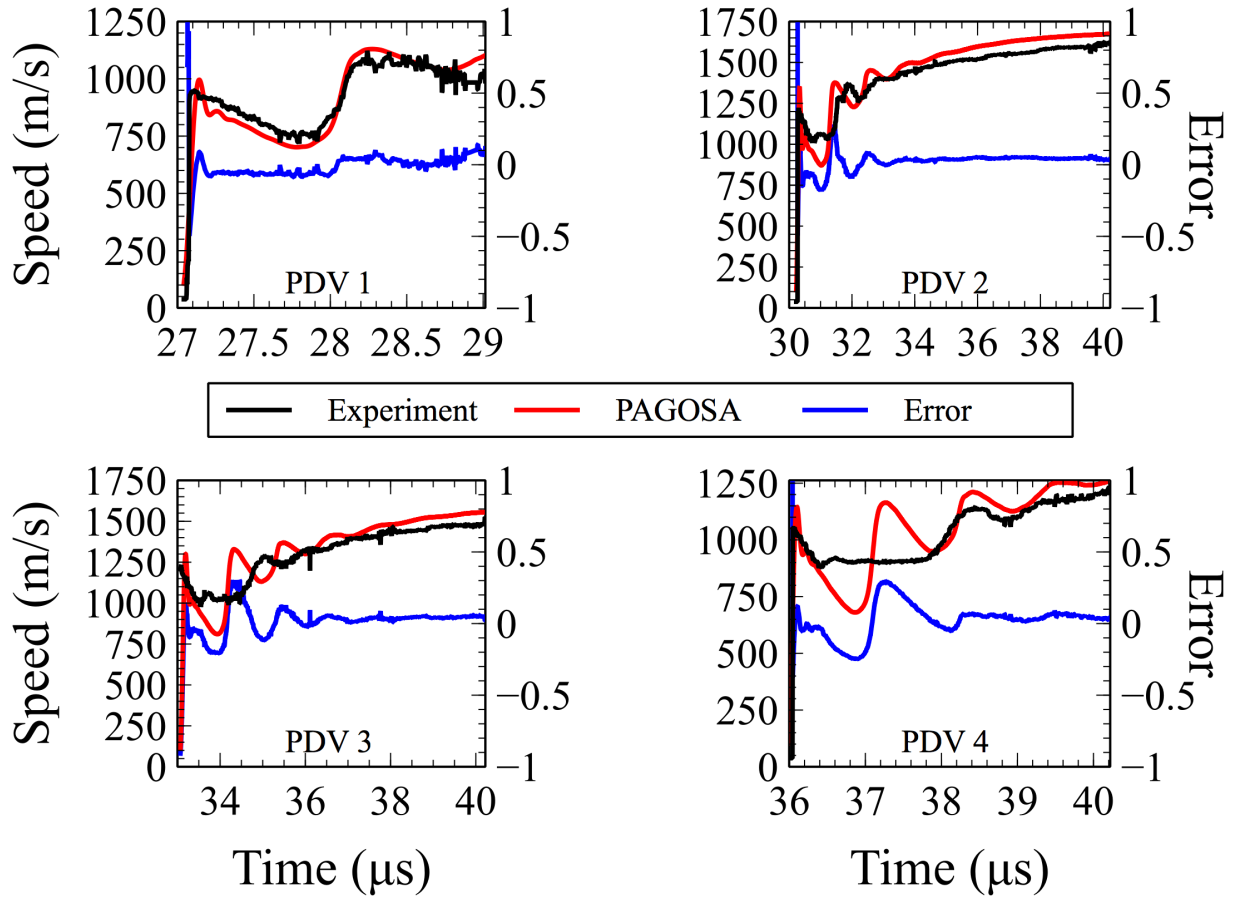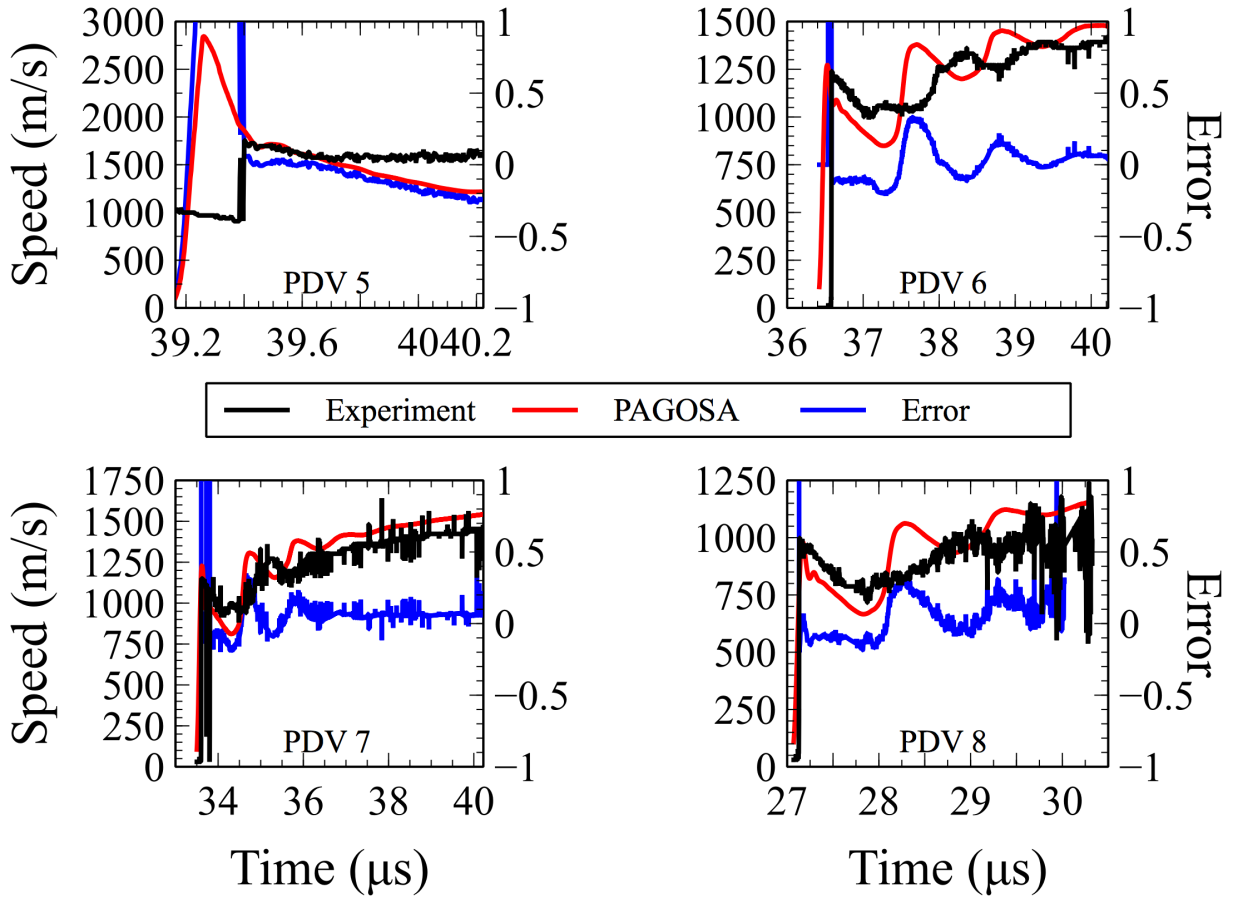
Figure 21. A comparison of experimental PDV signals with PAGOSA simulated PDVs for CYCLOPS I simulations using the Kospall strength model with the Johnson-Spall damage model for SS-304L confinement for (a) PDV 5, (b) PDV 6, (c) PDV 7, and (d) PDV 8

Preston-Tonks-Wallace (PTW)

The PTW model is a physically-based constitutive model that is strain rate and temperature dependent and is based on the computation of normalized shear stresses coupled with a von Mises yield criterion for a radial return to the yield surface. Figure 22 and Figure 23 directly compare the shifted PDV signals for the CYCLOPS I PAGOSA simulations using the PTW strength model for the SS-304L confinement. The PDV signals are shifted by 20.223 µs.

Again, each simulated PDV signal, with exception of PDV 5, captures the initial velocity spike and drop-off. Figures 24 and 25 compare the same PAGOSA simulation with the PTW model but with Johnson-Spall damage enabled. For the case with material damage, the PDV signals are shifted by 20.221 µs.

Figure 22. A comparison of experimental PDV signals with PAGOSA simulated PDVs for CYCLOPS I simulations using the PTW strength model for SS-304L confinement for (a) PDV 1, (b) PDV 2, (c) PDV 3, and (d) PDV 4

PTW
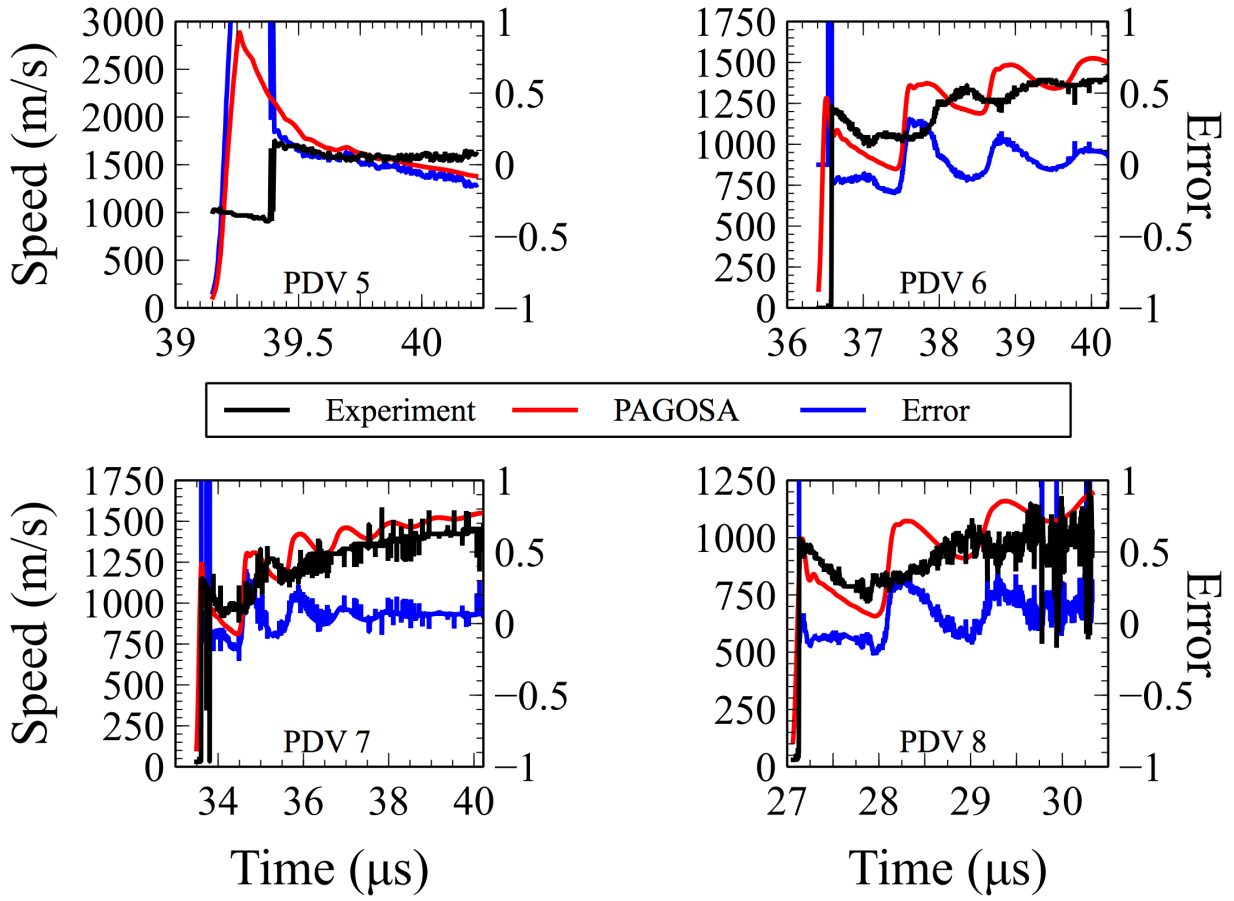
Figure 23. A comparison of experimental PDV signals with PAGOSA simulated PDVs for CYCLOPS I simulations using the PTW strength model for SS-304L confinement with Johnson-Spall damage enabled for (a) PDV 5, (b) PDV 6 (c) PDV 7, and (d) PDV 8
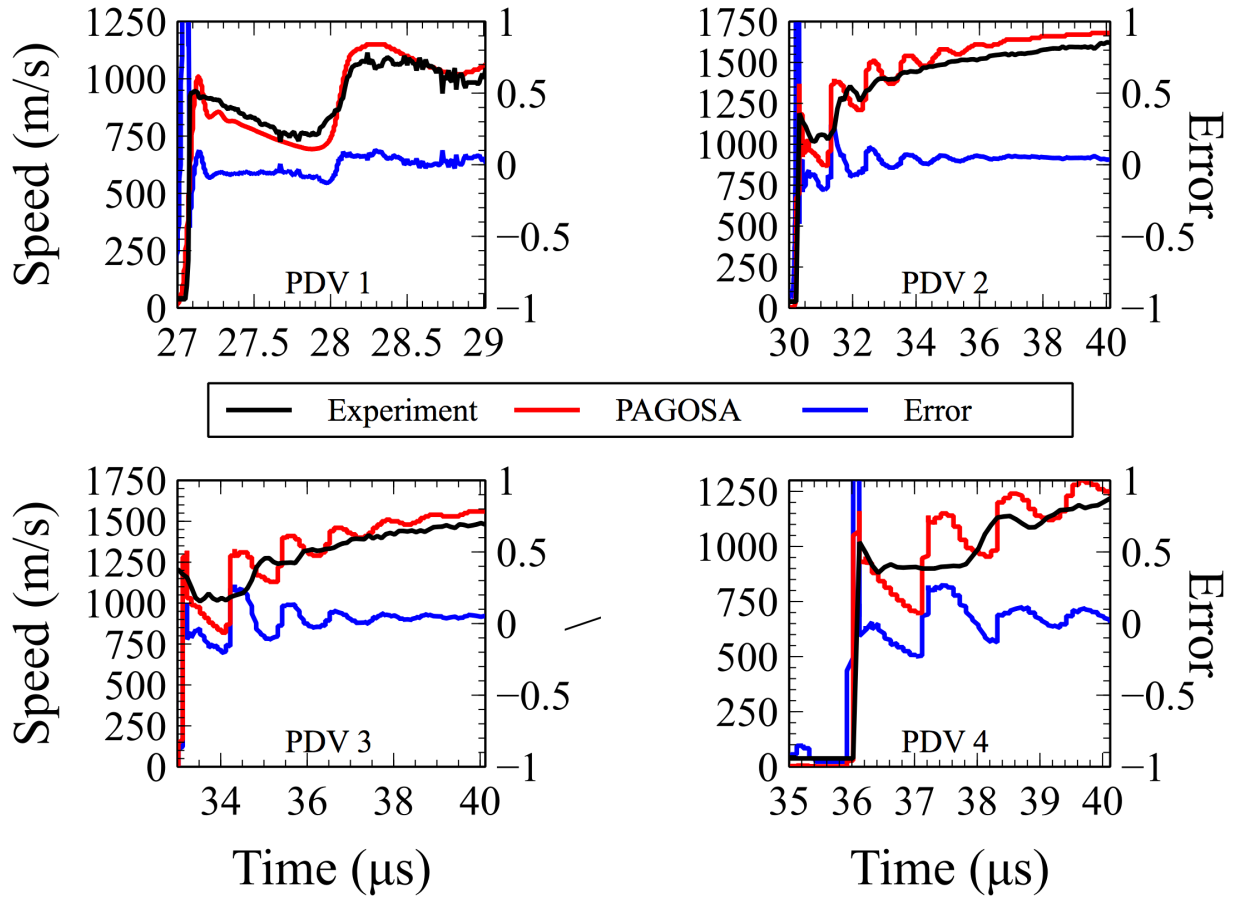
Figure 24. A comparison of experimental PDV signals with PAGOSA simulated PDVs for CYCLOPS I simulations using the PTW strength model with Johnson-Spall damage enabled for SS-304L confinement for (a) PDV 1, (b) PDV 2, (c) PDV 3, and (d) PDV 4
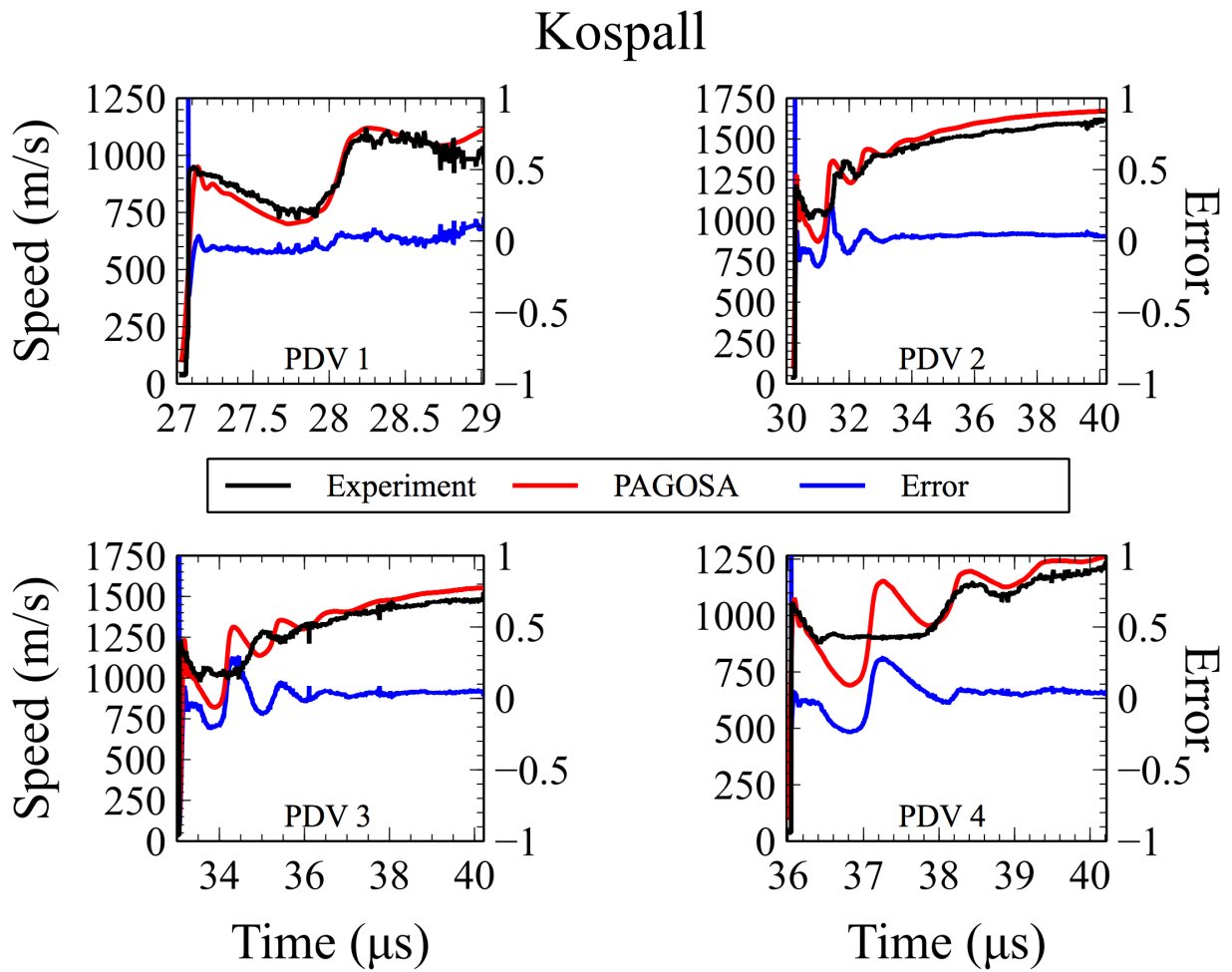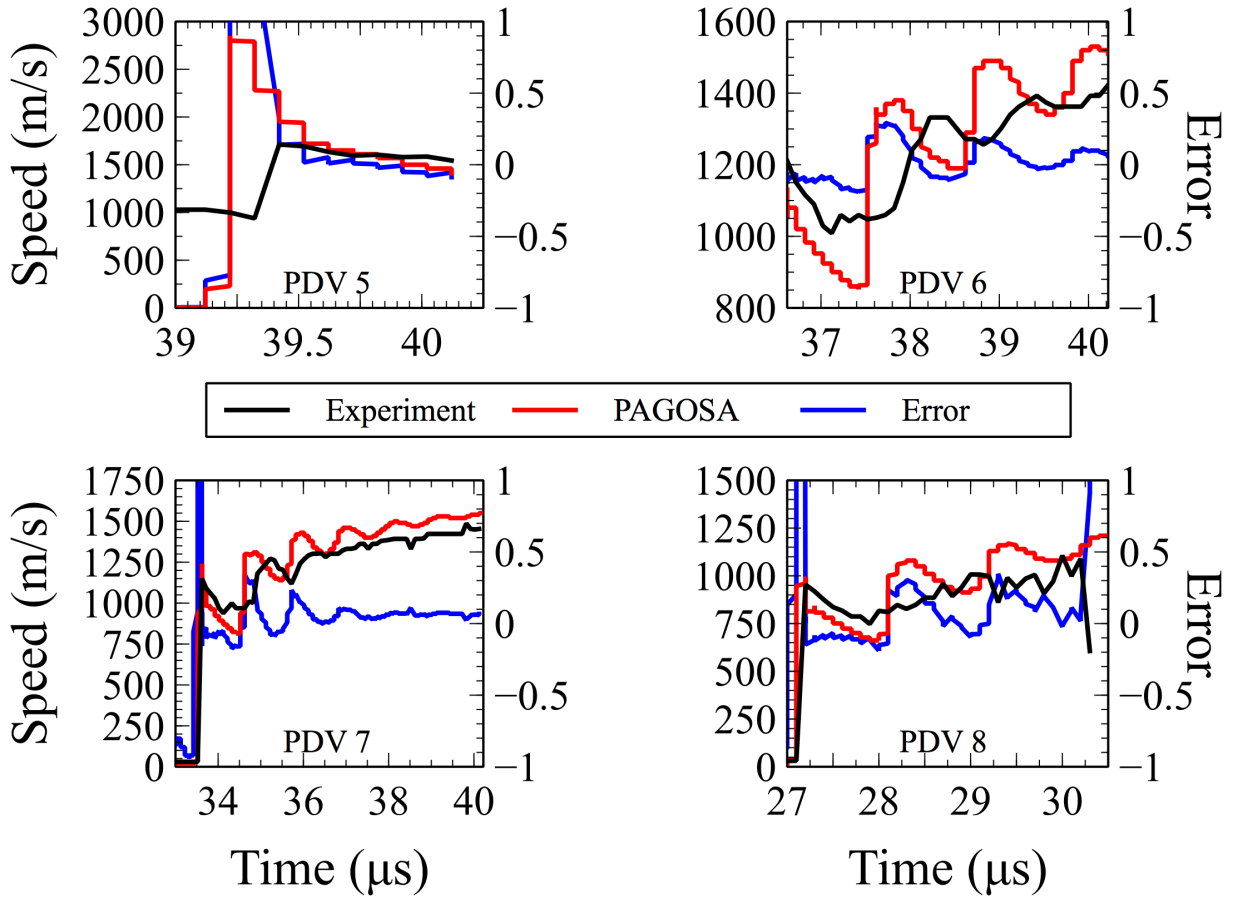
Figure 25. A comparison of experimental PDV signals with PAGOSA simulated PDVs for CYCLOPS I simulations using the PTW strength model with Johnson-Spall damage enabled for SS-304L confinement for (a) PDV 5, (b) PDV 6 (c) PDV 7, and (d) PDV 8

Steinberg-Cochran-Guinan (SG)

   The SG model used is a modified version for high strain rate applications and is based on equivalent plastic strain, internal energy, and pressure with dependency on strain rate and temperature. Figure 26 and Figure 27 directly compare the shifted PDV signals for the CYCLOPS I PAGOSA simulations using the SG strength model for the SS-304L confinement. The PDV signals are shifted by 20.231 µs.

   Each simulated PDV signal, with exception of PDV 5, captures the initial velocity spike and drop-off, however much like the other models, the signal tends to cycle above and below the experimental curves, especially for PDVs furthest from the booster. Figures 28 and 29 compare the same PAGOSA simulation with the SG model but with Johnson-Spall damage enabled. For the case with material damage, the PDV signals are shifted by 20.223 µs.
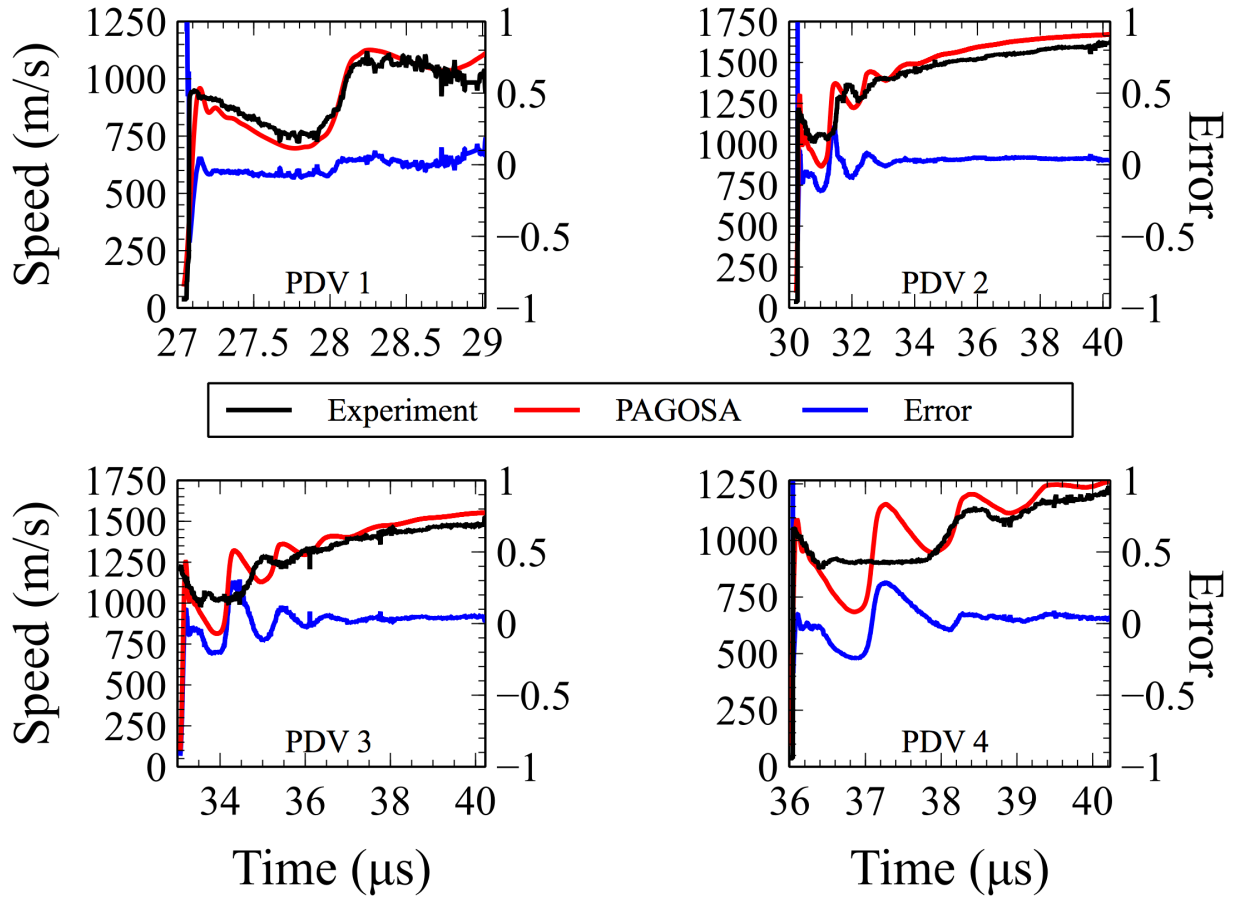
Figure 26. A comparison of experimental PDV signals with PAGOSA simulated PDVs for CYCLOPS I simulations using the SG strength model for SS-304L confinement for (a) PDV 1, (b) PDV 2, (c) PDV 3, and (d) PDV 4

SG
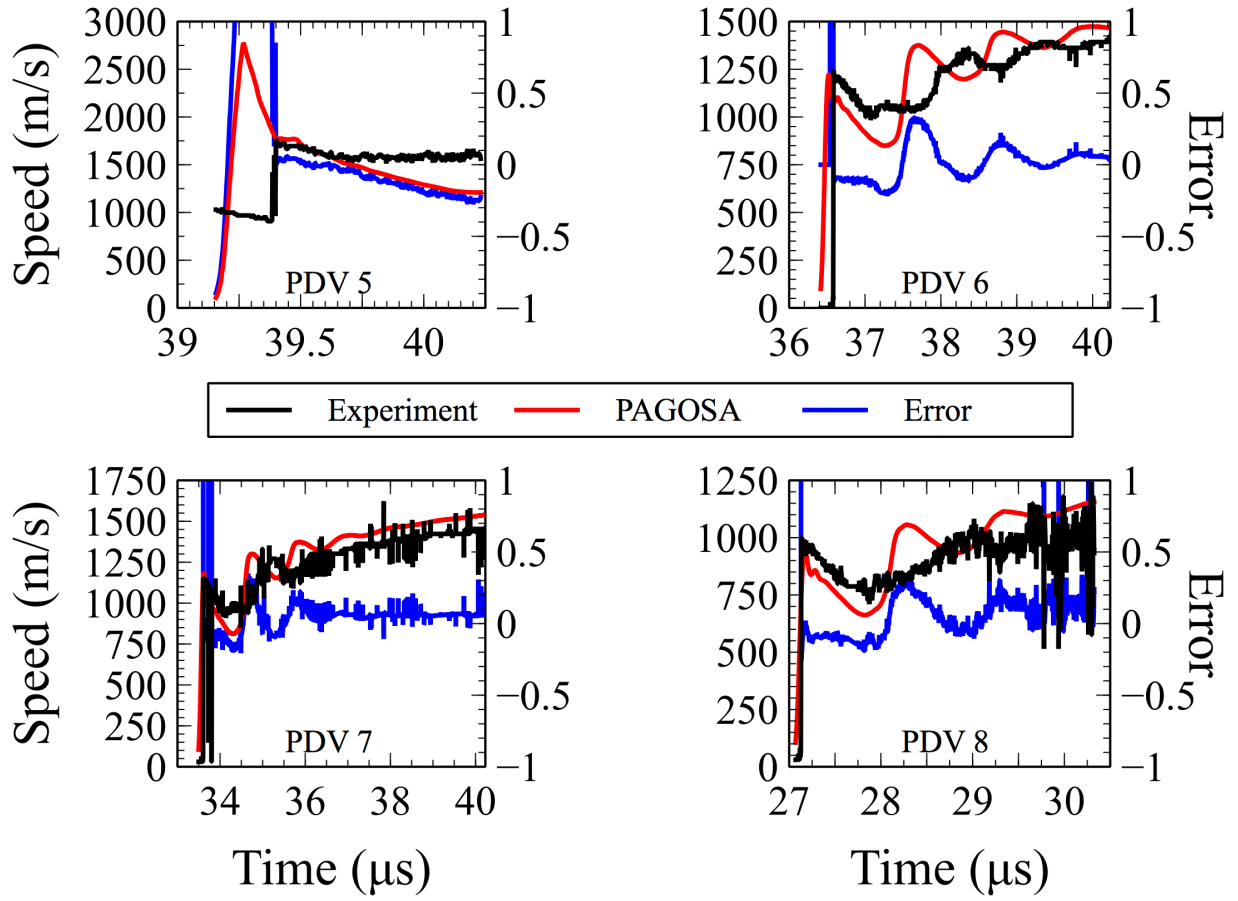
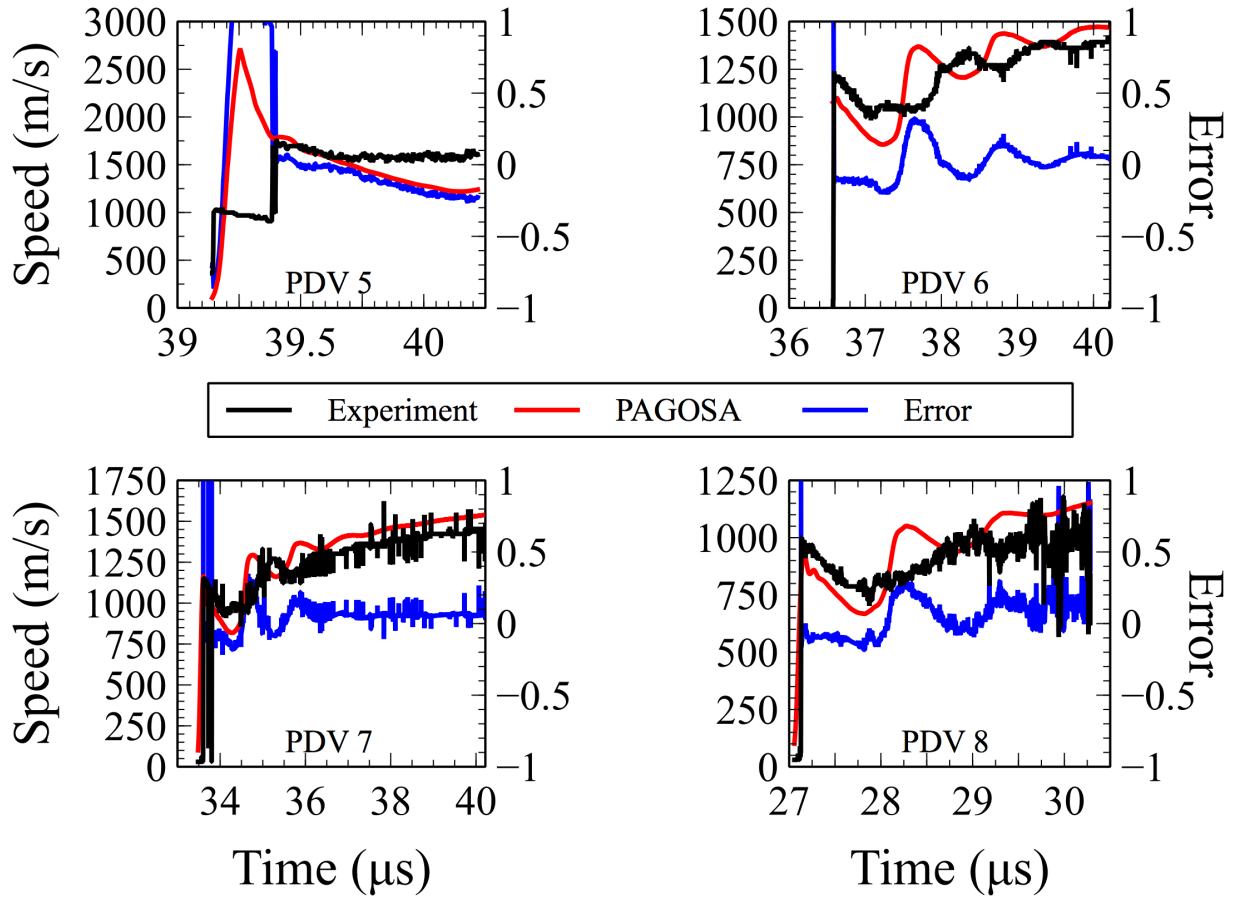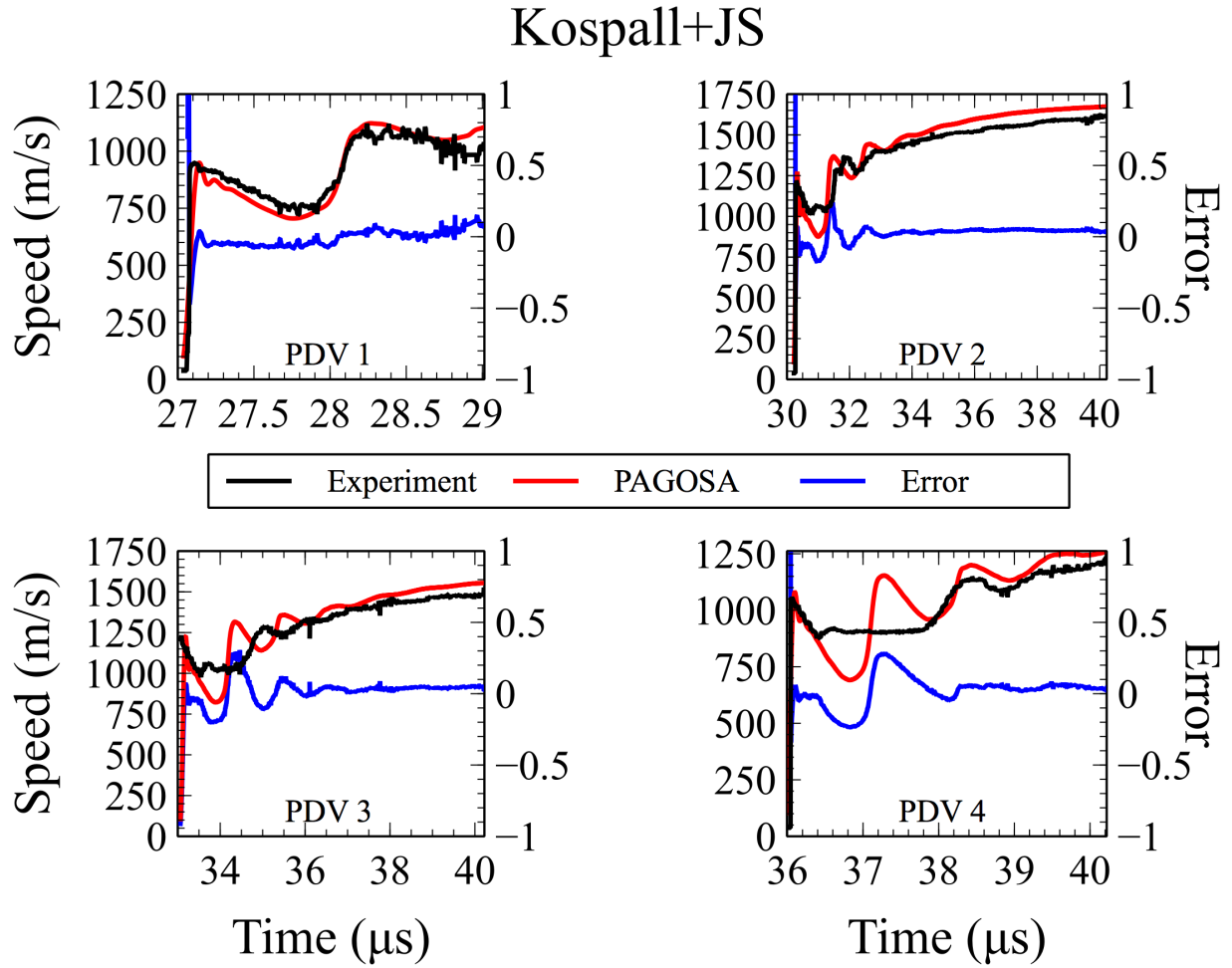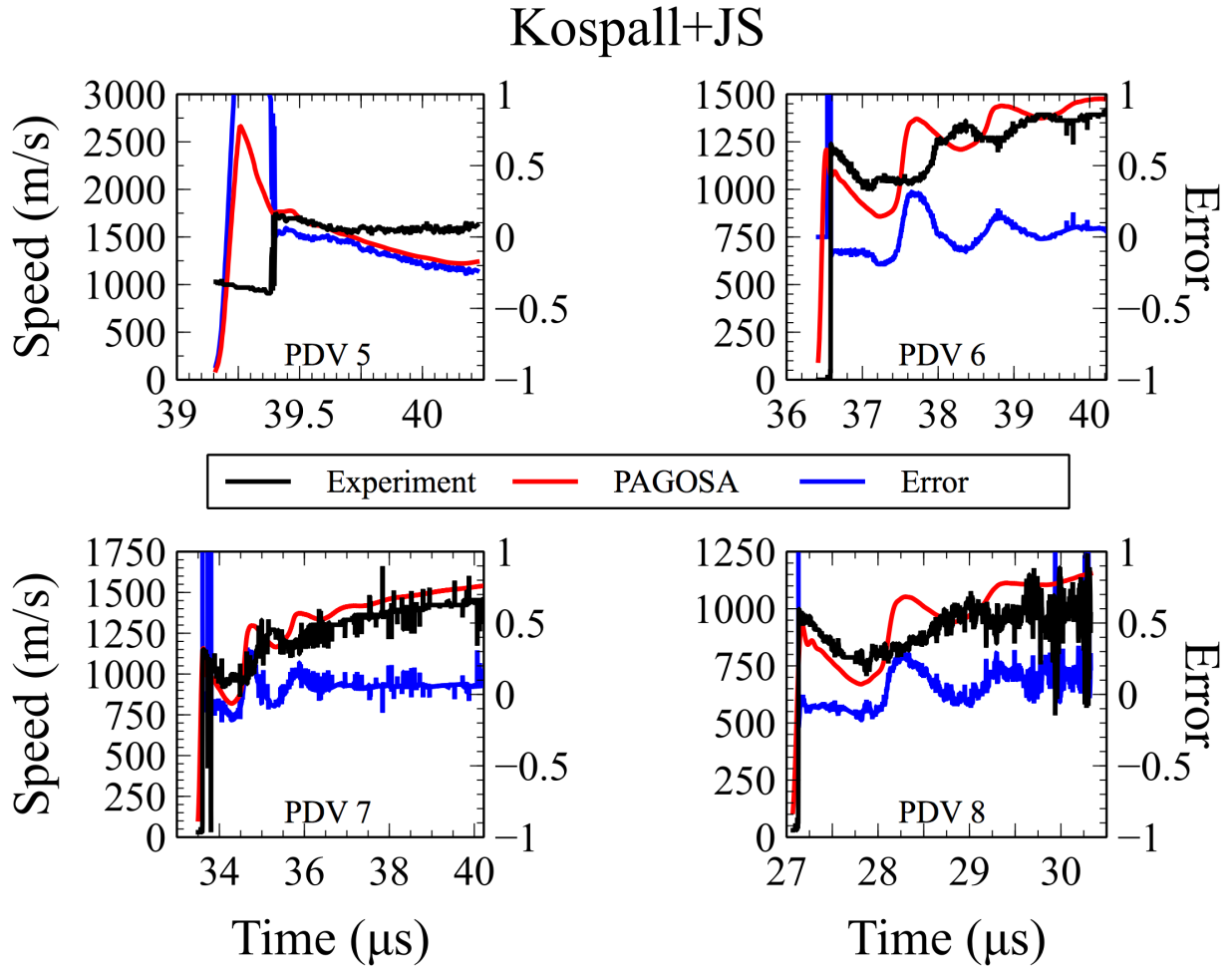Figure 27. A comparison of experimental PDV signals with PAGOSA simulated PDVs for CYCLOPS I simulations using the SG strength model for SS-304L confinement with Johnson-Spall damage enabled for (a) PDV 5, (b) PDV 6 (c) PDV 7, and (d) PDV 8
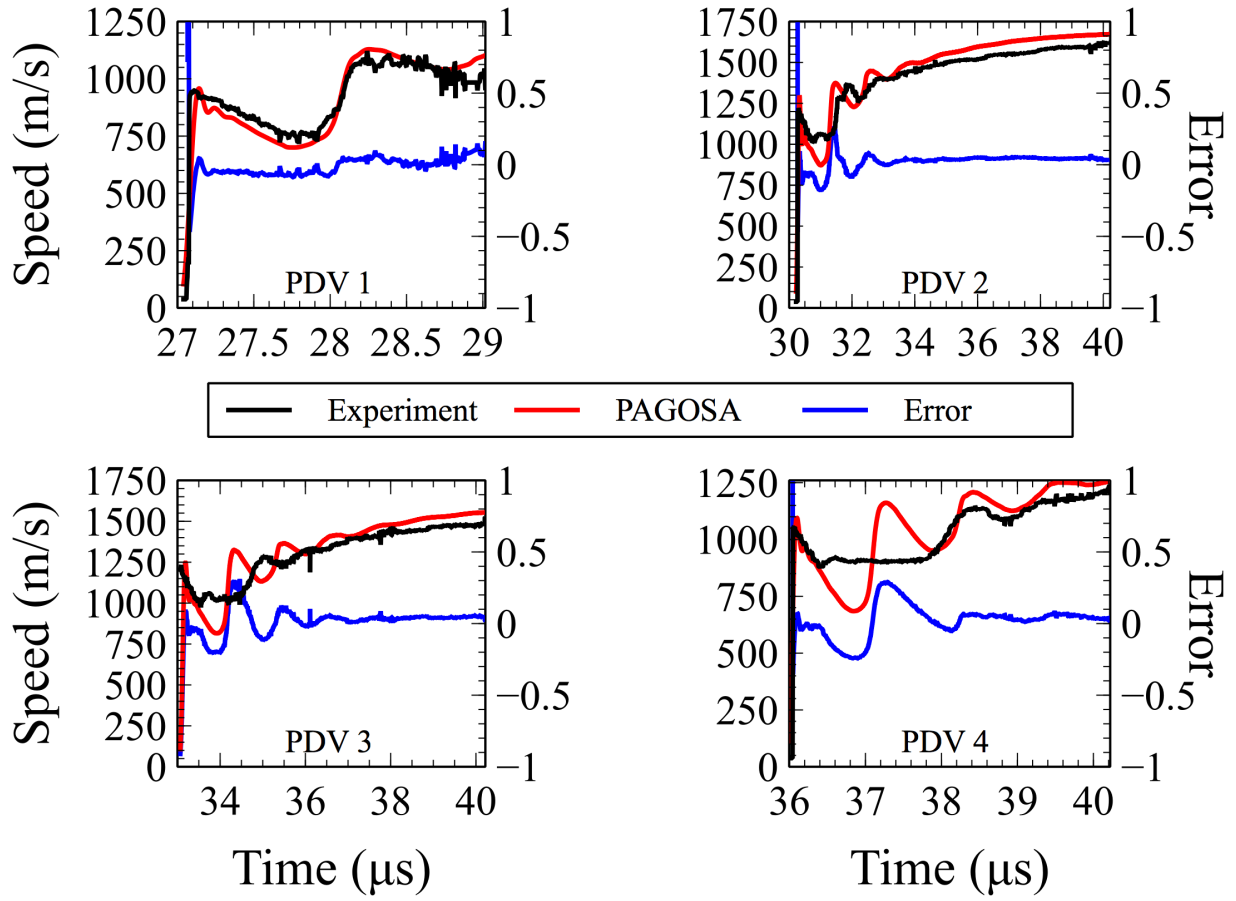
Figure 28. A comparison of experimental PDV signals with PAGOSA simulated PDVs for CYCLOPS I simulations using the SG strength model with Johnson-Spall damage enabled for SS-304L confinement for (a) PDV 1, (b) PDV 2, (c) PDV 3, and (d) PDV 4
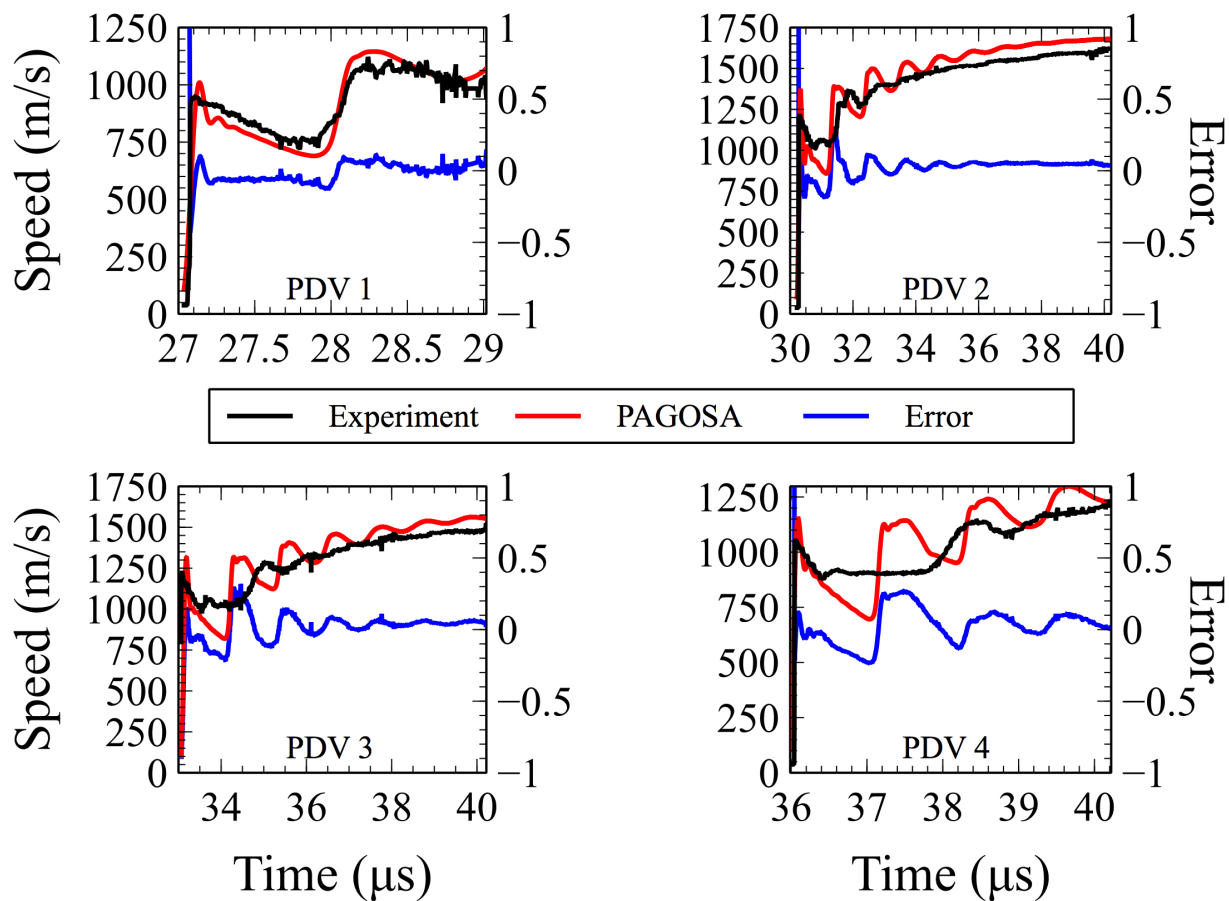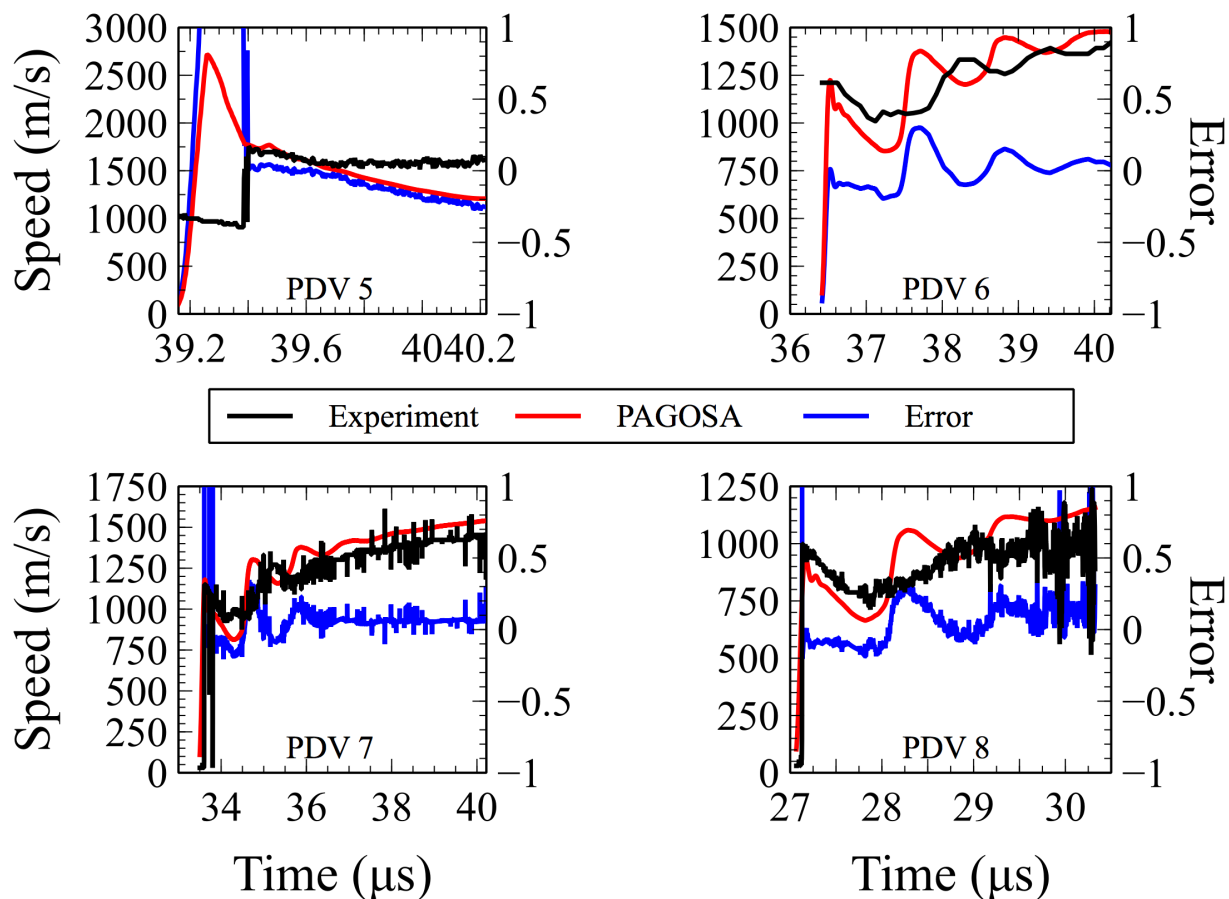
Figure 29. A comparison of experimental PDV signals with PAGOSA simulated PDVs for CYCLOPS I simulations using the SG strength model with Johnson-Spall damage enabled for SS-304L confinement for (a) PDV 5, (b) PDV 6 (c) PDV 7, and (d) PDV 8

Simulated PDV Error Summary

Figure 30 shows the effect of disabling or enabling the Johnson-Spall damage model for the stainless steel confinement. Overall, minimal difference is observed for most PDVs though the inclusion of damage considerably improves error for PDV 6. Tables 7 and 8 give the average PDV curve percent error with respect to the experimental proof shot without and with Johnson-Spall damage, respectively.
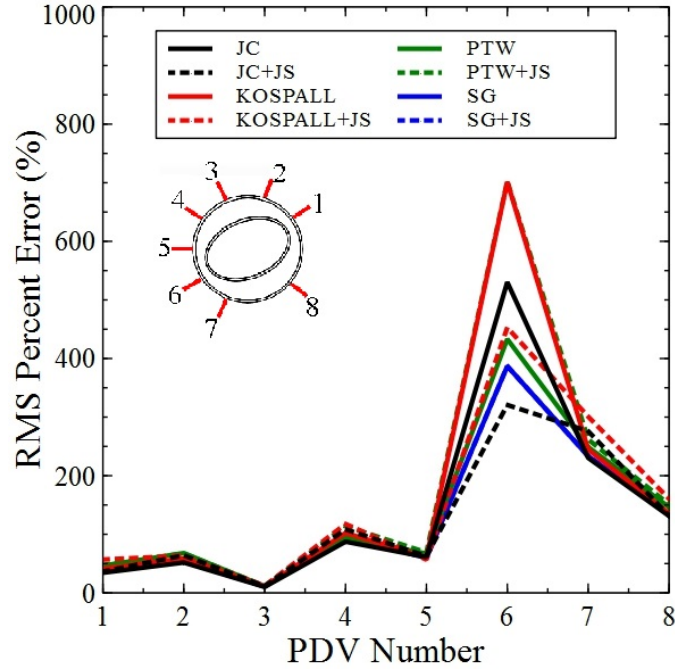
Figure 30. RMS error for each strength model at each simulated PDV

Table 7. Average percent error of the simulated PDV signals for each strength model

	Percent Error (%)			
PDV	JC	KOSPALL	PTW	SG
1	2.769	6.210	4.404	1.514
2	6.767	6.433	7.335	5.070
3	1.323	1.405	2.232	2.013
4	13.313	14.475	13.250	14.330
5	14.414	14.198	26.992	10.484
6	18.968	21.031	30.603	28.910
7	34.246	29.288	30.000	27.585
8	21.814	26.440	24.719	19.360

Table 8. Average percent error of the simulated PDV signals for each strength model with Johnson-Spall damage

	Percent Error (%)			
PDV	JC+JS	KOSPALL+JS	PTW+JS	SG+JS
1	2.534	3.706	4.228	3.197
2	5.723	6.176	7.311	5.808
3	1.761	1.482	2.741	2.162
4	9.969	11.808	10.841	11.320
5	13.215	14.746	24.395	13.191
6	25.260	34.649	25.504	20.028
7	26.274	28.980	28.385	25.958
8	21.087	22.194	23.515	21.620

Conclusions

The following conclusions can be made with regards to the accuracy of modeling the CYCLOPS I experiment:

- The FF burn model best reproduces the burn front timing for the PBX-9502 proton radiography experiments based on the global RMS error (6.33 sh, 200 μm mesh size) and global average timing calculations (1.71 sh, 200 μm mesh size) of PAGOSA simulations.
- The SURF burn models produces burn timing of similar accuracy to FF, but at a lower mesh size (150 μm). Due to the lower mesh size and resulting longer simulation time, the SURF burn model may not be viable for large simulations due to increased simulation times.
- The SG strength model without Johnson-Spall damage for the SS-304L confinement cylinder produces the lowest average error and second lowest RMS error for each simulated PDV signal when compared to the proof shot experimental PDV data.
- The inclusion of damage via the Johnson-Spall model for the SS-304L confinement cylinder makes minimal difference in RMS error for all strength models for all PDVs, except for PDV 6 which shows considerable improvement.

Future Work

More simulations of the CYCLOPS I shot will be performed to investigate modeling precision under uncertainty. Using the most accurate burn model and strength form, the input space will be systematically explored:

- Determine the acceptable range of variation for modeling parameters of the FF burn model and dual form JWL/Mie-Grüneisen equation of state.
- Develop a sampling routine for the JWL EOS to generate thermodynamically consistent parameter sets
- Use synthetic proton radiography (pRad) with 3D CYCLOPS simulations and compare with pRad experimental images
- Use a surrogate model coupled with an uncertainty quantification (UQ) routine to assess precision of burn front time-of-arrival predictions for the PAGOSA simulation framework.
- Use a surrogate model coupled with a sensitivity analysis (SA) routine to assess the major controlling factors to modeling uncertainty by computing the first order and total effect variance indices.

References

[1]   Terrones, G., Burkett, M.W., Morris, C., "Burn front and reflected shock wave visualization in an inertially confined detonation of high explosive," *Shock Compression of Condensed Matter*, AIP Conf. Proc 1426, pp239-242, 2012.

[2]   Saunder, A., "Proton radiography summary of 2015-2016 LANSCE run cycle," Los Alamos National Laboratory Technical Report LA-UR-16-23766.

[3]   Terrones, G., Burkett, M.W., Morris, C., "Burn front data from the CYCLOPS I experiment (U)," Los Alamos National Laboratory Technical Report LA-UR-11-07121

[4]   Terrones, G., "CYCLOPS proof shot (U)," Los Alamos National Laboratory Technical Report LA-UR-10-03963.

[5]   Terrones, G., Burkett, M.W., Morris, C., Oro, D., "CYCLOPS experiment (U)," Los Alamos National Laboratory Technical Report LA-UR-10-04469

[6]   Terrones, G., Burkett, M.W., Morris, C., "Burn front and reflected shock wave visualization in an inertially confined detonation of high explosive (U)," Los Alamos National Laboratory Technical Report LA-UR-11-03382.

[7]   Hodgson, A.N., "Modeling an IHE experiment with a suite of DSD models," *Journal of Physics: Conference Series*, Volume 500, 2014.

[8]   Aslam, T.D., Bdzil, J.B., Hill, L.G., "Extensions to DSD theory: Analysis of PBX-9502 rate stick data," *11th Symposium on Detonation*, pp21-29, 1998.

[9]   Hill, L.G., Aslam, T.D., "Detonation shock dynamics calibration for PBX-9502 with temperature, density, and material lot variations," *14th International Detonation Symposium*, 2010.

[10]   Handley, C.A., *Proceedings of the 13th International Detonation Symposium*, pp864-870, 2006.

[11]   Steinberg, D.J., Cochran, S.G., Guinan, M.W., "A constitutive model for metals applicable at high strain rate," *Journal of Applied Physics*, V51, pp1498-1504, 1980.

[12]   Johnson, G.R, Cook, W.H., "A constitutive model and data for metals subjected to large strains, high strain rates, and high temperatures," *Proceedings of the Seventh International Symposium on Ballistics*, The Hague, The Netherlands, pp541-548, 1983.

[13]   Steinberg, D.J., Guinan, M.W., "Constitutive relations for the KOSPALL code," Lawrence Livermore National Laboratory report UCID-16326, 1973.

[14]   Preston, D.L., Tonks, D.L, Wallace, D.C., "Model of plastic deformation for extreme loading conditions," *Journal of Applied Physics*, V93, pp211-223, 2003.

[15]   Johnson, J.N., "Dynamic fracture and spallation in ductile solids," *Journal of Applied Physics*, V52, pp2812-2825, 1981.

Appendix

Summary of Isochrone Lag Time Metrics

Table A.1. Summary of isochrone lag times in shakes (sh) for the upper region ($0 \leq \theta \leq \pi$) for a CYCLOPS simulation using the SURF burn model at a mesh size of 150 μm for isochrone positions of Table 1.

1st Isochrone	2nd Isochrone	3rd Isochrone	4th Isochrone	5th Isochrone
7.23	-7.26	-5.38	-2.90	15.07
-0.50	-11.34	-6.36	-6.26	8.18
0.09	-9.27	-5.14	-4.95	5.36
-0.50	-7.82	-4.18	-6.26	-1.35
-6.45	-8.09	-5.38	-7.40	-2.85
-8.83	-6.98	-9.69	-8.55	-4.17
-11.50	-8.38	-11.17	-8.32	-6.50
-9.72	-7.54		-5.61	-0.73
-8.53	-8.38			
-7.34	-6.98			
	-5.83			

6th Isochrone	7th Isochrone	8th Isochrone	9th Isochrone	10th Isochrone
15.36	16.10	14.10	19.40	16.50
5.21	7.60	9.60	17.20	14.20
1.56	7.30	7.10	13.50	8.20
5.42	3.31	4.80	17.00	2.20
2.98	4.28	3.10	12.10	5.40
-0.34	0.74	3.00	12.60	5.00
-1.81	-0.04	1.90	9.30	3.20
-3.05	-0.04	3.00	10.60	3.60
-2.02	-1.71	8.50	4.10	
-0.15	-1.32	8.90	4.10	
0.46	0.54	9.30	3.90	
-0.15	-0.73		7.20	
	-0.74			

11th Isochrone	12th Isochrone	13th Isochrone	14th Isochrone	15th Isochrone
14.50	11.20	11.90	10.80	4.90
6.40	10.00	14.00	10.60	8.60
2.40	21.40	9.90	9.90	8.60
5.90	13.20	6.20	11.50	8.80
10.80	3.10	4.80	11.20	0.90
10.50	3.10	7.30	10.60	3.40
11.00	3.10	10.70	13.50	6.00
12.40	4.40	9.50	13.00	10.20
10.30	2.80	14.00		
	1.50			

Table A.2. Summary of isochrone lag times in shakes (sh) for the upper region ($0 \leq \theta \leq \pi$) for a CYCLOPS simulation using the FF burn model at a mesh size of 200 μm for isochrone positions of Table 1.

1st Isochrone	2nd Isochrone	3rd Isochrone	4th Isochrone	5th Isochrone
6.98	-8.73	-6.73	-3.72	14.80
-2.18	-12.71	-7.52	-7.29	7.36
-1.78	-11.12	-6.33	-5.70	4.62
-3.37	-9.93	-5.53	-6.89	-1.66
-9.73	-11.12	-7.13	-8.09	-2.83
-12.12	-10.33	-11.90	-9.28	-4.01
-15.69	-11.91	-13.89	-9.28	-6.36
-14.11	-10.72		-6.50	-0.48
-13.71	-12.31			
-12.52	-11.12			
	-9.53			

6th Isochrone	7th Isochrone	8th Isochrone	9th Isochrone	10th Isochrone
15.82	15.60	14.40	19.00	16.20
4.24	7.00	9.40	17.00	13.90
0.85	6.25	5.80	13.10	7.60
4.60	2.84	4.30	16.60	1.80
3.12	4.73	2.30	12.30	5.70
-0.26	0.55	3.10	12.70	5.30
-1.80	0.16	2.70	9.20	3.00
-2.96	0.94	3.50	10.70	4.10
-1.03	-0.61	9.80	4.20	
0.48	-0.23	10.60	4.90	
1.23	1.29	10.20	4.90	
0.85	0.55		8.40	
	2.06			

11th Isochrone	12th Isochrone	13th Isochrone	14th Isochrone	15th Isochrone
14.60	11.50	12.70	13.00	6.80
7.20	10.70	15.10	12.30	9.40
2.00	22.20	11.50	11.60	10.20
6.40	14.10	7.60	13.70	11.00
11.10	3.60	6.80	13.30	3.40
10.30	3.60	8.80	13.30	6.40
10.30	4.00	11.90	15.90	9.00
12.30	5.10	11.10	15.50	13.20
9.90	2.40	15.10		
	0.90			

Table A.3. Summary of isochrone lag times in shakes (sh) for the upper region ($0 \leq \theta \leq \pi$) for a CYCLOPS simulation using the MSFF burn model at a mesh size of 300 μm for isochrone positions of Table 1.

1st Isochrone	2nd Isochrone	3rd Isochrone	4th Isochrone	5th Isochrone
22.04	12.18	18.83	25.12	46.32
14.91	7.44	17.05	20.36	39.78
16.10	9.81	17.65	21.55	37.40
16.69	11.59	19.42	19.77	29.67
13.12	12.77	19.42	18.58	27.29
13.12	15.73	14.68	16.79	24.32
11.34	15.14	13.50	17.39	22.53
17.29	16.92		19.77	27.88
21.45	18.10			
22.04	18.69			
	21.07			

6th Isochrone	7th Isochrone	8th Isochrone	9th Isochrone	10th Isochrone
51.61	55.00	57.00	65.40	66.40
41.50	46.10	52.90	63.60	61.70
35.55	44.30	46.90	57.70	55.20
39.12	39.60	44.00	60.10	48.10
37.93	40.20	41.60	54.10	49.90
33.76	36.00	41.00	54.10	47.50
30.79	36.60	41.60	50.00	45.10
29.60	36.60	42.20	52.40	45.10
30.19	34.20	46.90	44.10	
31.38	33.00	46.40	44.10	
31.98	34.80	46.40	45.30	
31.38	34.80		46.40	
	34.80			

11th Isochrone	12th Isochrone	13th Isochrone	14th Isochrone	15th Isochrone
66.80	66.80	72.40	72.50	72.50
58.00	66.20	72.40	71.90	74.30
51.50	75.70	67.10	70.70	72.50
55.60	66.20	62.30	71.30	72.50
58.00	55.60	59.90	69.50	63.60
56.80	55.00	62.30	69.50	65.40
56.20	52.00	65.30	70.70	67.80
56.20	54.40	62.30	71.30	71.30
55.00	50.80	66.50		
	49.00			

Table A.4. Summary of isochrone lag times in shakes (sh) for the lower region ($-\pi \leq \theta \leq 0$) for a CYCLOPS simulation using the SURF burn model at a mesh size of 150 μm for isochrone positions of Table 1.

1st Isochrone	2nd Isochrone	3rd Isochrone	4th Isochrone	5th Isochrone
10.20	5.69	7.72	6.53	6.62
10.20	5.69	6.49	4.52	4.91
4.26	4.53	1.06	2.29	4.91
4.55	0.25	-0.10	1.62	3.85
5.74	2.52	1.74	-0.64	3.64
1.87	5.97	-0.10	-0.64	0.99
-1.99	2.24	-0.82	2.29	2.24
-0.80	2.24	-2.46	4.09	0.54
-1.99	-0.03	-6.85	0.04	0.99
-0.80	-0.03	-7.81	-2.65	0.54
-4.96			-2.42	0.33
-7.04			-2.90	-2.23
-8.53			-1.08	-2.01

6th Isochrone	7th Isochrone	8th Isochrone	9th Isochrone	10th Isochrone
8.89	-0.22	3.00	-3.50	0.60
5.63	1.45	5.00	2.80	0.00
6.23	1.82	8.30	3.90	-4.00
7.45	1.11	6.30	7.60	-4.60
7.66	-1.03	0.60	9.50	-0.80
7.24	-3.01	-1.70	7.90	-0.30
2.98	-3.01	1.20	6.40	
-2.02	-5.00	0.90	1.90	
-1.81	-5.00	-4.40	7.70	
1.02	-4.25	-4.40		
3.42	0.54	-5.00		
		-3.30		

11th Isochrone	12th Isochrone	13th Isochrone	14th Isochrone	15th Isochrone
4.60	-6.70	-0.50	-3.60	-10.60
3.40	-3.40	2.10	3.50	-7.50
3.40	-0.50	-3.10	-3.20	-3.20
2.40	-2.40	-3.90	-2.60	-7.10
3.20	4.20	-0.50	-5.40	-8.40
5.30		-3.60	-4.20	-8.60
7.30			1.60	-6.30
3.80			2.50	-4.20
				0.30

Table A.5. Summary of isochrone lag times in shakes (sh) for the lower region (-π ≤ θ ≤ 0) for a CYCLOPS simulation using the FF burn model at a mesh size of 200 μm for isochrone positions of Table 1.

1st Isochrone	2nd Isochrone	3rd Isochrone	4th Isochrone	5th Isochrone
8.57	4.39	6.00	6.14	6.58
8.17	4.39	5.20	3.38	4.22
1.81	2.80	-0.30	1.43	5.01
1.81	-2.37	-1.55	1.03	4.22
2.60	-0.78	-0.36	-1.34	3.44
-1.78	2.01	-2.34	-0.95	1.09
-6.55	-2.37	-4.34	1.43	2.27
-6.15	-3.56	-6.73	2.98	0.31
-8.14	-7.14	-11.90	-1.34	0.70
-8.14	-7.14	-13.89	-4.51	-0.09
-13.32			-4.91	-0.87
-15.69			-5.70	-3.22
-17.29			-4.91	-3.22

6th Isochrone	7th Isochrone	8th Isochrone	9th Isochrone	10th Isochrone
8.90	-0.60	3.00	-0.80	0.90
5.57	1.34	4.10	2.70	-0.20
6.31	2.10	8.30	4.20	-3.20
7.76	1.34	6.10	8.00	-4.70
8.52	0.19	4.90	10.20	0.20
8.15	-2.13	-0.50	9.10	0.20
3.67	-1.76	2.60	7.20	
-1.21	-3.63	2.60	3.00	
-0.84	-3.28	-2.80	9.40	
1.78	-2.51	-2.80		
4.05	2.51	-2.80		
		-0.90		

11th Isochrone	12th Isochrone	13th Isochrone	14th Isochrone	15th Isochrone
4.80	-6.70	1.60	-2.00	-9.80
3.80	-2.60	3.40	5.10	-6.20
3.40	0.60	-1.50	-1.60	-1.10
2.80	-1.20	-2.30	-0.80	-5.00
3.40	4.80	1.20	-3.60	-7.00
5.90		-1.90	-2.40	-7.00
7.40			3.50	-3.80
4.10			5.10	-1.50
				2.90

Table A.6. Summary of isochrone lag times in shakes (sh) for the lower region ($-\pi \leq \theta \leq 0$) for a CYCLOPS simulation using the MSFF burn model at a mesh size of 300 μm for isochrone positions of Table 1.

1st Isochrone	2nd Isochrone	3rd Isochrone	4th Isochrone	5th Isochrone
26.80	26.99	33.06	35.22	39.78
27.99	27.50	31.28	34.62	36.21
23.23	26.99	26.54	30.47	36.21
25.61	23.44	25.95	29.87	34.43
27.39	29.36	28.91	27.50	33.83
27.39	35.88	28.91	28.09	31.45
24.42	34.69	30.69	31.06	33.24
28.58	38.84	29.50	32.84	30.86
30.36	39.43	30.10	30.47	32.64
36.30	42.39	29.50	28.68	32.64
38.67			29.28	32.64
45.20			30.47	31.45
48.16			32.84	32.05

6th Isochrone	7th Isochrone	8th Isochrone	9th Isochrone	10th Isochrone
43.28	39.00	44.00	41.70	49.30
41.50	40.20	45.80	47.00	46.30
39.72	38.40	48.70	47.60	42.20
40.90	37.20	45.80	51.80	39.20
41.50	36.00	45.20	53.00	44.00
39.72	33.00	38.60	50.60	42.80
36.15	31.80	39.20	47.00	
30.79	30.10	38.60	43.50	
30.79	30.70	32.70	4.60	
33.76	30.10	32.70		
37.33	35.40	32.10		
		33.90		

11th Isochrone	12th Isochrone	13th Isochrone	14th Isochrone	15th Isochrone
58.00	49.00	59.30	60.60	56.50
55.00	5.00	62.30	66.00	58.80
53.80	54.40	55.20	60.60	61.80
51.50	50.20	54.00	59.40	58.80
53.20	57.30	56.40	55.30	55.90
52.70		51.60	55.80	55.30
54.40			61.20	58.20
52.10			63.00	60.60
				64.20

Summary of PBX-9502 Model Constants

Table A.7. SURF burn model constants for PBX-9502

Variable	Value
burncon(1)	0.001
burncon(2)	0.999
burncon(3)	0.055
burncon(4)	0.24
burncon(5)	6
burncon(6)	43298.11835590
burncon(7)	-35356.9929246
burncon(8)	11721.06027920
burncon(9)	-2015.70898175
burncon(10)	216.2064452280
burncon(11)	-12.3288500067
burncon(12)	1.0
burncon(13)	0.5
A	-3.1
B	0.28
P_0	2.5
P_1	21.5
df_1	3.0
n	0.0
C	0.0

Table A.8. FF burn model constants for PBX-9502

Variable	Value
bf_cut_{min}	0.01
bf_cut_{max}	0.99
bp_cut_{min}	0.0
bp_cut_{max}	0.285
n	6.0
a_5	43298.11835590
a_4	-35356.9929246
a_3	11721.0607920
a_2	-2015.70898175
a_1	216.2064452280
a_0	-12.3288500067
Q_{lim}	1.0
W_{min}	0.5

Table A.9 MSFF burn model constants for PBX-9502

Variable	Value
bf_cut_{min}	0.01
bf_cut_{max}	0.99
bp_cut_{min}	0.0
bp_cut_{max}	0.285
n	6.0
a_5	43298.11835590
a_4	-35356.9929246
a_3	11721.0607920
a_2	-2015.70898175
a_1	216.2064452280
a_0	-12.3288500067
Q_{lim}	1.0
P_shk_{min}	0.000001
P_shk_{max}	0.055
Q_shk_{min}	0.000001
dQ_{min}	0.0
$P_{reshock}$	10.3
W_{min}	0.5

Summary of SS-304L Model Constants

Table A.10. JC strength model constants for SS-304L

Variable	Value
B	0.01175
C	0.03
n	0.65
m	0.825
E_{melt}	8.81e-03
E_{room}	0.0
$\gamma`$	2.26

Table A.11. KOSPALL strength model constants for SS-304L

Variable	Value
α	32.0
β	0.29
b	2.5974026
h	-4.5454545e-04
q	1.0
f	0.002
g	300.0

Table A.12. PTW strength model constants for SS-304L

Variable	Value
θ_0	0.015
p	5.0
s_0	0.00705
s_∞	0.0065
κ	0.3
γ	0.0001
y_0	0.0031
y_∞	0.0007
y_1	0.0705
y_2	0.46
β	0.25
α	0.23
T_{melt}	1808.0
A	55.9

Table A.13. SG strength model constants for SS-304L

Variable	Value
α	43.0
ε_0^p	0.0
β	0.35
δ	0.001
E_m	8.81e-03
γ	2.26
$\gamma^`$	2.26

Table A.14. Johnson-Spall damage model constants for SS-304L

Variable	Value
α_0	1.00088
α_s	0.77
η	0.1
ν	0.29